ISLAMIC UNIVERSITY OF TECHNOLOGY

MODELING OF FREQUENCY DEPENDENT PERMITTIVITY OF MATERIALS AND SIMULATION OF PLASMONIC NANOSTRUCTURES USING FDTD ALGORITHM

By

Kh. Arif Shahriar (102458)

Md. Mahamudun Arif Joy (102474)

Ikramul Hasan Sohel (102476)

Co-supervised By

Md. Ghulam Saber

Lecturer,

Department of Electrical and Electronic Engineering,

Islamic University of Technology.

Supervised By

Rakibul Hasan Sagor

Assistant Professor,

Department of Electrical and Electronic Engineering,

Islamic University of Technology.

Declaration of Authorship

We, Kh. Arif Shahriar (102458), Md. Mahamudun Arif Joy (102474) and Ikramul Hasan Sohel (102476) declare that this thesis titled 'Modeling of frequency dependent permittivity of materials and simulation of plasmonic nanostructures using FDTD algorithm' has been done for the partial fulfillment of the degree of Bachelor of Science in Electrical and Electronic Engineering at Islamic University of Technology. No part of this thesis has been submitted anywhere else for obtaining any degree. We have provided appropriate references to different published works which we have consulted.

Submitted By:

Kh. Arif Shahriar (102458)

Md. Mahamudun Arif Joy (102474)

Ikramul Hasan Sohel (102476)

MODELING OF FREQUENCY DEPENDENT PERMITTIVITY OF MATERIALS AND SIMULATION OF PLASMONIC NANOSTRUCTURES USING FDTD ALGORITHM

Approved By

Md. Ghulam Saber

Thesis Co - supervisor,
Lecturer,

Department of Electrical and Electronic Engineering,

Islamic University of Technology.

Rakibul Hasan Sagor

Thesis Supervisor,

Assistant Professor,

Department of Electrical and Electronic Engineering,

Islamic University of Technology.

Prof. Dr. Md. Shahid Ullah

Head of the Department,

Department of Electrical and Electronic Engineering,

Islamic University of Technology.

Acknowledgements

First of all, we would like to express our deepest gratitude to Almighty Allah (SWT) who has blessed us with the opportunity and ability to do this work.

We are grateful to our thesis supervisor, Rakibul Hasan Sagor sir for creating a friendly and comfortable environment for us. His generous inspiration and guidance helped us a lot to overcome the difficulties we faced during our work.

We would also like to thank our thesis co-supervisor Mr. Md. Ghulam Saber, Lecturer, Department of EEE, IUT for sharing his experience and knowledge generously with us.

We also would like to thank all the faculty members of the Department of EEE, IUT for their support.

We are also thankful to our family and friends for their support and well-wishes.

Abstract

Speed of modern digital circuits is limited by the delay caused in electronic interconnects due to distributed RC effect. The diffraction limit of ordinary light waves limits the resolution of optical instruments like microscopes. Surface Plasmon Polaritons (SPP) can be used to overcome both this drawbacks. But the major problem is that SPP propagation cannot be sustained beyond micrometers. As a result it has become a great field of research interest in recent years. One of the objectives of this thesis is to find out a method to extract modeling parameters of materials so that they can be used for simulation of plasmonic structures. Besides, we have developed a simulation model for simulating plasmonic structures and simulated different structures using this model.

Table of Contents

List of figures

List of tables

Chapter 1

Introduction and Background

1.1 Introduction

Our scientific understanding of the universe depends to a large extent on how much we can observe the different natural phenomena occurring around us. This need has brought into existence a good variety of optical instruments, from microscopes to observe the tiny to telescopes to see the titanic. The world economy today is largely based on information flow around the globe through transcontinental optical fiber. Many of the constraints of existing technologies can be overcome using light as the carrier of information. But classically it is believed that a fundamental limit on our ability to put light to use is set by the wavelength of light itself. Propagating waves of any type whether they are sound waves, light waves, radio waves etc. cannot be focused to a dimension smaller than half of the wavelength [1]. This limit is commonly referred to as the diffraction limit.

The wavelength range for visible light is from 400 to 750nm [2]. So, photons needed for devices having dimensions in nanometer scale are not in the visible range of the electromagnetic wave spectrum if the above mentioned limitation is maintained. This would keep optics out of nanoscience and nanotechnology and hence the concept of "nano-optics" would never go nano in reality.

But nano-optics today is no more an unimplementable concept. Today we know that light does not mean freely propagating waves only, rather evanescent electromagnetic waves bound to the surfaces of objects can also exist at optical frequencies [1]. These evanescent waves cannot carry energy away from the object as they decay rapidly. These are therefore called the near field of the object. One important property of this near field is that it is not bound by the aforesaid diffraction limit. As a result such evanescent waves can be confined to dimensions on the atomic scale. So, if we can convert optical energy into such evanescent waves then it can be used in devices having nano-scale dimensions. This is the fundamental idea behind nano-optics and this is where Plasmonics enters the picture.

When light is incident on a metal nanoparticle, the electrons in the particle are pushed to one side by the incident electric field. So positive charges are accumulated at one side of the particle and negative charges on the other side, giving rise to an attractive force between them. If the negative charge were suddenly released it would undergo periodic oscillations with a certain frequency. If this natural resonance frequency is matched with the frequency of the incident light then all the free electrons in the metal would undergo large oscillations. Due to this simultaneous oscillation of many electrons, large electric fields are produced at the immediate vicinity of the particle which again reinforce the oscillation. This leads to a coupled excitation which consists of two different oscillations- electromagnetic field oscillating just outside the particle and charges oscillation inside the particle [1]. This coupled excitation is known as localized surface plasmon polariton resonance (LSPPR) or simply plasmon resonance, a fundamental concept in Plasmonics.

In simple words, surface plasmon potaritons (SPP) are electromagnetic waves with a unique property that they propagate along the interface of metal and dielectric only. Plasmonics is the study of surface plasmons and its applications.

Plasmonic devices can be used to overcome the problems faced with Very Large Scale Integration (VLSI) technology. In VLSI technology, one fundamental need is to minimize the device dimensions so that electrons need to travel short distances and hence the device can operate fast. But there are two basic problems with this miniaturization. First, the integrated circuits (ICs) face reliability problem due to miniaturization. Second, miniaturized ICs require more sophisticated and complicated cooling systems.

Even if these problems associated with individual ICs are solved, there remains a major problem in exchanging signals between cascaded ICs. Due to distributed RC effect [3], there is delay in signal propagation through copper wire interconnects connecting the ICs.

The generated heat and signal propagation delay affect the speed of digital circuits heavily. This limitation has become more evident as the annual increase rate of microprocessor clock speed has become stagnant in recent years [4].

So, to improve the situation, faster interconnects are required. Optical interconnects like fiber optic cable can carry digital data with a capacity that is 1000 times greater than that of electronic interconnects. But they are also about 1000 times larger [5].

So, it is very difficult to combine the two technologies on the same circuit. The ideal solution would be to have a single nanoscale circuit that can carry both electric currents and optical signals. Plasmonic circuits offer the potential to carry electric currents and optical signals through the same thin metal circuitry, thereby allowing a combination of the technical advantages of photonics and electronics on the same chip.

In general, plasmonic devices can operate very fast (the good thing from photonics), being very small at the same time (the good thing from electronics) as SPPs can overcome diffraction limit.

But the main limitation is that the decay rate of plasmons is very fast [6]. Researches are going on to overcome this problem using metamaterials (a metamaterial is a material with special properties derived from its structure rather than its chemical composition) rather than natural materials.

Researches are going on to use plasmonics in cancer treatment also. The proposed technology uses nanoshells composed of 100 nanometer wide silica particles with an outer layer of gold.

The nanoshells , once injected into the bloodstream, will be guided to the tumour by antibodies bound to the shell surface. At certain infrared wavelengths, human and animal tissues are transparent to radiation. So, when near-infrared laser light is shone on the skin above the tumorous region, it would penetrate the skin, reach the tumour and get absorbed to create plasmons in the gold shells. The cancer cells would get heated up and would be destroyed thermally leaving the surrounding healthy tissue unharmed.

Experiments following this principle have already been performed on mice at the Rice University in Houston, Texas, USA. In the mice treated with nanoshells, all signs of cancer disappeared within only 10 days [7].

Another potential application of plasmonics is Colorimetric Plasmon Resonance Imaging (CPRI). A CPRI device, (also called nano Lycurgus Cup Array or nanoLCA) is actually nothing but arrays of billions of nanoscale Lycurgus cups planted in a piece of cheap, ordinary plastic of the size of a postage stamp. When substances are poured into the cups, they display a range of colors which can be used to identify the substance. Researchers at the University of Illinois have already designed and tested a prototype nanoLCA [8]. Once this technology becomes available, then instead of highly expensive, bulky equipments like spectrometers, scientists will be able perform a range of tests on the spot using a nanoLCA device in their cellphones. Using nanoLCA, urine or saliva samples will be able to be tested for the presence of antibodies or pathogens; liquid samples will be able to be tested for chemical or biological agents and explosives at border crossings at very low costs.

Perhaps the most fascinating potential application of plasmonics would be the invention of an invisibility cloak. In 2006 John B. Pendry and his colleagues at the Imperial College London theoretically showed that a shell of metamaterials could re-route the electromagnetic waves travelling through it, diverting them around a central cavity within [9]. Recently a group of researchers at the California Institute of Technology developed a metamaterial that has a negative index for the blue-green region of the visible spectrum of light and thus could be used for invisibility cloaking [9]. The cloaking device would be a thick shell of metamaterials that could bend electromagnetic radiation around its central cavity. So, an observer would see only the objects behind it.

Although an invisible man may not become a reality in recent future, such ideas illustrate the rich array of optical properties that inspire researchers in the plasmonics field.

Plasmonics can also be used in several ways to make more efficient and cost-effective solar cells. Today, solar cells use a good amount of silicon. As silicon is an expensive material, there is significant research into thin-film silicon solar cells that use less silicon to reduce the cost of solar panels. However, as the silicon regions get thinner, less incident light is absorbed. To solve this problem, metal nanoparticles can be used on the surface of thin film silicon solar cells [10]. Advances in this sector can benefit countries like Bangladesh greatly as the low efficiency and high cost of solar panels is still a bar to its application on a mass scale.

To fulfill the promise offered by plasmonics, more research needs to be done in these areas. Besides emergence of plasmon based devices, which are considerably smaller than the propagating light's wavelength, plasmonics is expected to be the key nanotechnology that will combine electronic and photonic components on the same chip in coming years.

1.2 Literature Review

The research in the field of plasmonics started as early as 1950. But it is only recently that research in this arena has gained considerable momentum. In the last decade, Surface-Plasmon-Polaritons (SPPs) have drawn much attraction as a field of research resulting in many published works. Another significant field of research is modeling of frequency dependent properties of materials. Plasmon enhanced solar cells and LED have also gained considerable attention in recent times. This literature review focuses on works published on these topics.

The modeling parameters of several materials have been reported till date to our knowledge. Deinega et al. [11] have reported the modified Lorentz model parameters for silicon applicable in the wavelength range of 300-1000 nm. Rakic et al. [12] have reported the parameters for 11 materials using Brendel-Bormann and Lorentz-Drude model. Sagor et al. [13] have reported the Modified Debye Model parameters for Nickel, Palladium, Iridium, Titanium and Hexagonal Cobalt. Saber et al. [14] determined the Modified Debye and Lorentz Model parameters for Cuprous Oxide and Silicon-Germanium alloy. Alsunaidi et al. [15] have reported the parameters for AlGaAs. M.A. Ordal et al. [16] have reported the modeling parameters for 14 metals applicable for the infrared and far infrared region.

Geometry of optoelctronic devices differ from each other due to bends, splitters and recombinations. Several works of SPP propagation associated with these different structures have been reported to our knowledge. FDTD based simulation of waveguides made of nanoparticles in the visible range is presented by W. M. Saj [17]. Experimental study of the propagation of plasmons on gold nanowires is done by T. Onuki et al. [18]. Hochberg et al. [19] studied surface plasmon waveguides for near infrared light from the viewpoint of design, fabrication and characterization and explained how efficient coupling of light between conventional silicon waveguides and plasmonic waveguides can be done using compact couplers. A unique property of plasmons is the ability to bend with the metal. K. Hasegawa et al. studied the effect of curvature on the propagation of plasmons [20].

X. Zhai et al. [21]studied a ring resonator based plasmonic waveguide filter. The transmission characteristics of SPPs in ring resonator have been studied by T.-B. Wang, et al. [22].

J. Vuckovic et al., [23] proposed a method for enhancing the emission from LEDs by coupling surface plasmons. The applicability of localized surface plasmons to enhance the absorbance in silicon based solar cells has been studied by S. Pillai, et al. [24]. A review on the theoretical and experimental progress made so far in the study of plasmon enhanced solar cells has been presented by K. Catchpole et al. [10].

1.3 Thesis Organization

The thesis has been organized in the following way:

In **Chapter 2,** the theory of SPP propagation has been discussed and the mathematical formulations of SPP propagation at single and double interfaces have been derived.

In **Chapter 3,** the mathematical models commonly used for approximating the frequency dependent permittivity of materials have been discussed.

In **Chapter 4,** the FDTD algorithm has been introduced. Since the original algorithm proposed by Yee ignores the frequency dependent properties of materials, we have used the Auxiliary Differential Equation (ADE) based algorithm for our simulation which has been discussed in this chapter. This chapter also discusses the absorbing boundary condition.

In **Chapter 5,** an optimization algorithm based on the Nelder-Mead method has been discussed and the modeling parameters of several materials have been extracted.

In **Chapter 6,** the simulated results of different plasmonic nanostructures are presented.

In **Chapter 7,** the concluding remarks about this work and our future plans with it are discussed.

Chapter 2

Theory of SPP propagation

2.1 Maxwell's Equations of Macroscopic Electromagnetism

Like any other electromagnetic phenomena, propagation of SPP along metal-dielectric interface is also governed by Maxwell's equations. For macroscopic electromagnetism, the equations can be expressed in terms of Gauss's Law, Faraday's Law and Ampere's Law. Details of the forthcoming derivations are available in [25].

Gauss's Law for electric field says that for a charge-free region, the divergence of electric flux density is equal to zero. That is,

$$\nabla . \mathrm{D} = 0 \tag{2.1}$$

Similarly, for magnetic field,

$$\nabla . \mathrm{B} = 0 \tag{2.2}$$

Ampere's Law says that the time derivative of electric field flux density is equal to the curl of magnetic field. That is,

$$\frac{\partial \mathrm{D}}{\partial \mathrm{t}} = \nabla \times \mathrm{H} \tag{2.3}$$

Faraday's Law says that the time derivative of magnetic field flux density is equal to the curl of the electrical field. That is,

$$\frac{\partial \mathrm{B}}{\partial \mathrm{t}} = -\nabla \times \mathrm{E} \tag{2.4}$$

Here,

E is the electric field vector (V/m).
D is the electric flux density vector (C/m^2).
H is the magnetic field vector (A/m).
B is the magnetic flux density vector (Wb/m^2).

If the electric and magnetic properties of materials are considered independent of direction, frequency and field i.e. if the materials are considered tobe isotropic, non-dispersive and linear then we can relate B to H and D to E as follows:

$$D = \varepsilon E \tag{2.5}$$

$$B = \quad H \tag{2.6}$$

where

ε is the electric permittivity (F/m) of the material

is the magnetic permeability (H/m) of the material

Using the values of E and H obtained from (2.5) and (2.6), we can rewrite (2.3) and (2.4) as follows:

$$\frac{\partial H}{\partial t} = -\frac{1}{\mu}\nabla \times E \tag{2.7}$$

$$\frac{\partial E}{\partial t} = \frac{1}{\varepsilon}\nabla \times H \tag{2.8}$$

2.2 The EM (electromagnetic) Wave Equation

From Maxwell's equations we can derive the EM wave equation which describes the field amplitude in time and space.

Taking the curl of (2.7) we get

$$\nabla \times (-\ \frac{\partial H}{\partial t}) = \nabla \times \nabla \times E \tag{2.9}$$

$$\Rightarrow -\ \frac{\partial}{\partial t}(\nabla \times H) = \nabla \times \nabla \times E \tag{2.10}$$

$$\Rightarrow -\ \frac{\partial}{\partial t}(\varepsilon\frac{\partial E}{\partial t}) = \nabla \times \nabla \times E \ \ \text{[From (2.8)]} \tag{2.11}$$

$$\Rightarrow -\mu\varepsilon(\frac{\partial^2 E}{\partial t^2}) = \nabla \times \nabla \times E \tag{2.12}$$

[Since ε is independent of time, so it is taken out of the time derivative]

$$\Rightarrow -\mu\varepsilon(\frac{\partial^2 E}{\partial t^2}) = \nabla(\nabla.E) - \nabla^2 E \tag{2.13}$$

Now, from (2.1), $\nabla.D = 0 \Rightarrow \nabla.\varepsilon E = \varepsilon(\nabla.E) = 0 \ \ \Rightarrow \nabla.E = 0$

Therefore, from (2.13),

$$-\mu\varepsilon(\frac{\partial^2 E}{\partial t^2}) = 0 - \nabla^2 E \tag{2.14}$$

$$\Rightarrow \nabla^2 E - \mu\varepsilon(\frac{\partial^2 E}{\partial t^2}) = 0 \tag{2.15}$$

Eq. 2.15 represents the wave equation for electric field. Similarly, the wave equation for magnetic field can be expressed as follows:

$$\nabla^2 H - \mu\varepsilon(\frac{\partial^2 H}{\partial t^2}) = 0 \tag{2.16}$$

So, the general form of EM wave equation is:

$$\nabla^2 U - \frac{1}{v_p^2}(\frac{\partial^2 U}{\partial t^2}) = 0 \tag{2.17}$$

where $v_p = \frac{1}{\sqrt{\mu\varepsilon}}$ represents the phase velocity of the wave. If the wavelength and time period of the wave are represented by λ and T respectively, then

$$v_p = \frac{\lambda}{T} \tag{2.18}$$

If the EM wave is harmonic in time and the wave propagation direction is x, then the general solution of the wave equation in complex form can be expressed as follows:

$$\psi(t, x) = Ae^{-j\omega t}e^{j\beta x} \tag{2.19}$$

where

$\psi(t, x)$ represents the value of the wave at time t and position x

$\omega = \frac{2\pi}{T}$ represents the angular oscillation (rad/s)

$\beta = \frac{2\pi}{\lambda}$ represents the angular phase (rad/m)

$$\therefore \frac{\omega}{\beta} = \frac{\lambda}{T} \Rightarrow v_p = \frac{\omega}{\beta} = \frac{\lambda}{T} \quad \text{[From (2.18)]} \tag{2.20}$$

Now, the electric and magnetic field vectors can be expressed in terms of three components directed along the three axes of the Cartesian co-ordinate system as shown below:

$$E = E_x . \overrightarrow{a_x} + E_y . \overrightarrow{a_y} + E_z . \overrightarrow{a_z} \tag{2.21}$$

$$H = H_x.\ \overrightarrow{a_x} + H_y.\overrightarrow{a_y} + H_z.\ \overrightarrow{a_z} \qquad (2.22)$$

Therefore, solving Ampere's Law, we get the equations for the components of the electric field along x,y and z directions as follows:

$$\frac{\partial E_x}{\partial t} = \frac{1}{\varepsilon}\left(\frac{\partial H_z}{\partial y} - \frac{\partial H_y}{\partial z}\right) \qquad (2.23)$$

$$\frac{\partial E_y}{\partial t} = \frac{1}{\varepsilon}\left(\frac{\partial H_x}{\partial z} - \frac{\partial H_z}{\partial x}\right) \qquad (2.24)$$

$$\frac{\partial E_z}{\partial t} = \frac{1}{\varepsilon}\left(\frac{\partial H_y}{\partial x} - \frac{\partial H_x}{\partial y}\right) \qquad (2.25)$$

Similarly, solving Faraday's Law, we get the equations for the components of the magnetic field along x,y and z directions as follows:

$$\frac{\partial H_x}{\partial t} = \frac{1}{\mu}\left(\frac{\partial E_y}{\partial z} - \frac{\partial E_z}{\partial y}\right) \qquad (2.26)$$

$$\frac{\partial H_y}{\partial t} = \frac{1}{\mu}\left(\frac{\partial E_z}{\partial x} - \frac{\partial E_x}{\partial z}\right) \qquad (2.27)$$

$$\frac{\partial H_z}{\partial t} = \frac{1}{\mu}\left(\frac{\partial E_x}{\partial y} - \frac{\partial E_y}{\partial x}\right) \qquad (2.28)$$

During the propagation of EM wave, the electric and magnetic fields remain perpendicular to each other.

2.3 SPP Propagation at Single Interface

The single, flat metal-dielectric interface is the simplest geometry that can be used for propagation of SPP. Let ε_m and ε_d represent the permittivities of metal and dielectric respectively.

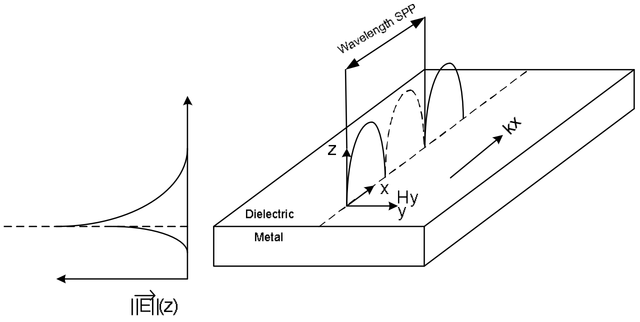

Fig. 2-1 SPP propagation at single interface

We assume that the fields have no variation in the z direction and hence all partial derivatives with respect to z are equal to zero. Two different modes of EM wave propagation, TE (Transverse Electric) and TM (Transverse Magnetic) are considered. Unlike classical definition, in FDTD, TE and TM modes are defined with respect to the plane of simulation rather than the plane of incidence.

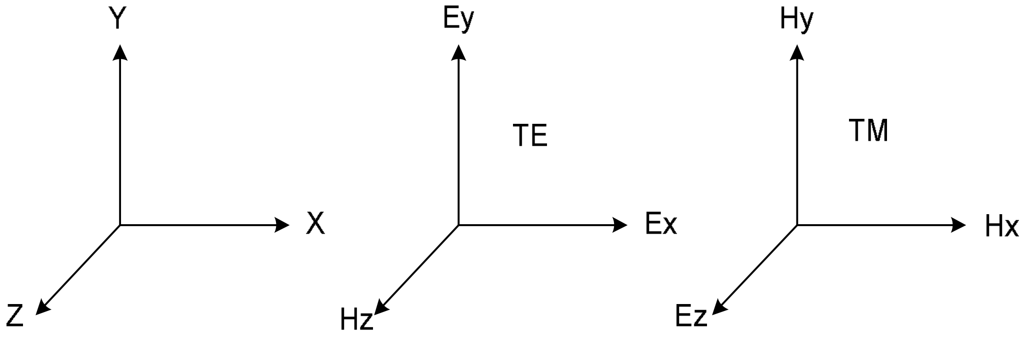

Fig. 2-2 Definitions of TE and TM modes

The equations for electric and magnetic fields in TE mode are

$$\frac{\partial E_x}{\partial t} = \frac{1}{\varepsilon}\frac{\partial H_z}{\partial y} \tag{2.29}$$

$$\frac{\partial E_y}{\partial t} = -\frac{1}{\varepsilon}\frac{\partial H_z}{\partial x} \tag{2.30}$$

$$\frac{\partial H_z}{\partial t} = \frac{1}{\mu}\left(\frac{\partial E_x}{\partial y} - \frac{\partial E_y}{\partial x}\right) \tag{2.31}$$

Similarly, the equations for electric and magnetic fields in TM mode are

$$\frac{\partial H_x}{\partial t} = \frac{1}{\mu}\frac{\partial E_z}{\partial y} \tag{2.32}$$

$$\frac{\partial H_y}{\partial t} = \frac{1}{\mu}\frac{\partial E_z}{\partial x} \tag{2.33}$$

$$\frac{\partial E_z}{\partial t} = \frac{1}{\varepsilon}\left(\frac{\partial H_y}{\partial x} - \frac{\partial H_x}{\partial y}\right) \tag{2.34}$$

For TE mode we assume H_z as time-harmonic field propagating in the x direction and exponentially decaying in the y direction.

$$H_z = Ae^{-j\omega t}e^{j\beta x}e^{k|y|} \tag{2.35}$$

For harmonic time dependence $\frac{\partial}{\partial t} = -j\omega$. The derivatives along the x and y directions can be found by multiplication by jβ and k respectively. So, from (2.29) we get

$$-j\omega E_x = \frac{k}{\varepsilon}H_z \tag{2.36}$$

$$\Rightarrow E_x = \frac{Ak}{-j\omega\varepsilon}e^{-j\omega t}e^{j\beta x}e^{ky} \tag{2.37}$$

Similarly,

$$E_y = -\frac{A\beta}{-j\omega\varepsilon}e^{-j\omega t}e^{j\beta x}e^{ky} \tag{2.38}$$

Since the fields tangential to the interface are continuous, so in the dielectric the tangential electric and magnetic fields are:

$$E_x = \frac{A_d k_d}{-j\omega\varepsilon_d}e^{-j\omega t}e^{j\beta x}e^{k_d y} \tag{2.39}$$

$$H_z = A_d e^{-j\omega t}e^{j\beta x}e^{k_d y} \tag{2.40}$$

Similarly, in metal the tangential electric and magnetic fields are:

$$E_x = \frac{-A_m k_m}{-j\omega\varepsilon_m} e^{-j\omega t} e^{j\beta x} e^{-k_m y} \quad (2.41)$$

$$H_z = A_m e^{-j\omega t} e^{j\beta x} e^{k_m y} \quad (2.42)$$

To make the H_z in (2.40) and (2.42) equal, the required condition is

$$A_d = A_m \quad (2.43)$$

Similarly, to make the E_x in (2.39) and (2.41) equal, the required condition is

$$\frac{k_d}{k_m} = -\frac{\varepsilon_d}{\varepsilon_m} \quad (2.44)$$

From (2.44) we see that the two permittivities need to be opposite in sign (one positive and one negative) for propagation to happen. Besides, in both media, the wave equation has to be satisfied and the propagation constants have to be same. Substituting H_z from (2.40) into the wave equation (2.16) we get

$$-\beta^2 H_z + k_d^2 H_z + \mu\varepsilon_d\omega^2 H_z = 0 \quad (2.45)$$

$$\Rightarrow \beta^2 = k_d^2 + \mu\varepsilon_d\omega^2 \quad (2.46)$$

Similarly, for metal

$$\beta^2 = k_m^2 + \mu\varepsilon_m\omega^2 \quad (2.47)$$

Substituting (2.44) in (2.46) we get

$$\beta^2 = (\frac{\varepsilon_d}{\varepsilon_m})^2 k_m^2 + \mu\varepsilon_d\omega^2 \quad (2.48)$$

$$\Rightarrow -(\frac{\varepsilon_d}{\varepsilon_m})^2\beta^2 = -(\frac{\varepsilon_d}{\varepsilon_m})^2 k_m^2 - (\frac{\varepsilon_d}{\varepsilon_m})^2\mu\varepsilon_m\omega^2 \quad (2.49)$$

Combining (2.48) and (2.49) we get

$$\beta^2\left(1 - \left(\frac{\varepsilon_d}{\varepsilon_m}\right)^2\right) = (\varepsilon_d - \left(\frac{\varepsilon_d}{\varepsilon_m}\right)^2 \varepsilon_m)\mu\omega^2 \quad (2.50)$$

$$\Rightarrow \beta^2\left(1 - \frac{\varepsilon_d}{\varepsilon_m}\right)\left(1 + \frac{\varepsilon_d}{\varepsilon_m}\right) = (1 - \frac{\varepsilon_d}{\varepsilon_m})\mu\varepsilon_d\omega^2 \quad (2.51)$$

$$\Rightarrow \beta^2 = \frac{\mu\varepsilon_d\omega^2}{1+\frac{\varepsilon_d}{\varepsilon_m}} \quad (2.52)$$

$$\Rightarrow \beta^2 = \frac{\mu\varepsilon_d\varepsilon_m\omega^2}{\varepsilon_m+\varepsilon_d} \quad (2.53)$$

$$\Rightarrow \beta = \omega\sqrt{\frac{\varepsilon_m\varepsilon_d}{\varepsilon_m+\varepsilon_d}} \tag{2.54}$$

Here, β is the phase constant for the propagating SPPs.

The derivation for TM mode can be started by considering E_z which is expressed as follows:

$$E_z = Ae^{-j\omega t}e^{j\beta x}e^{k|y|} \tag{2.55}$$

Using the same steps followed for E_x we can find out the expression for H_x

$$\frac{\partial H_x}{\partial t} = -\frac{1}{\mu}\frac{\partial E_z}{\partial x} \tag{2.56}$$

$$\Rightarrow -j\omega H_x = -\frac{k}{\mu}E_z \tag{2.57}$$

$$\Rightarrow H_x = \frac{k}{j\omega\mu}E_z \tag{2.58}$$

Similarly, for H_y ,

$$\frac{\partial H_y}{\partial t} = \frac{1}{\mu}\frac{\partial E_z}{\partial x} \tag{2.59}$$

$$\Rightarrow -j\omega H_y = -\frac{j\beta}{\mu}E_z \tag{2.60}$$

$$\Rightarrow H_y = \frac{\beta}{\omega\mu}E_z \tag{2.61}$$

Since H_x and E_z are tangential to the interface so they are continuous at the interface for the dielectric side,

$$H_x = \frac{A_d k_d}{j\mu\omega}e^{-j\omega t}e^{j\beta x}e^{k_d y} \tag{2.62}$$

$$E_z = A_d e^{-j\omega t}e^{j\beta x}e^{k_d y} \tag{2.63}$$

For the metal side,

$$H_x = -\frac{A_m k_m}{j\mu\omega}e^{-j\omega t}e^{j\beta x}e^{-k_m y} \tag{2.64}$$

$$E_z = A_m e^{-j\omega t}e^{j\beta x}e^{k_m y} \tag{2.65}$$

To make the E_z in (2.63) and (2.65) equal, the required condition is

$$A_d = A_m \tag{2.66}$$

Similarly, to make the H_x in (2.62) and (2.64) equal, the required condition is

$$Ak_d = -Ak_m \tag{2.67}$$

$$\Rightarrow A(k_d + k_m) = 0 \tag{2.68}$$

In order to have decaying fields from the interface towards the metal and dielectric layers, k has to be greater than zero. Therefore, there is no SPP in the TM mode if the TE and TM modes are defined as mentioned above. This definition of TE and TM modes can be found in [26].

2.4 SPP Propagation at Double Interface

The Metal-Dielectric-Metal (MDM) and Dielectric-Metal-Dielectric (DMD) structures are the two most common double interface configuration used for SPP propagation. In these structures SPPs are formed on both interfaces. If the decay distance is greater than the distance, a coupled mode of SPPs is formed due to interaction of fields from both sides [6, 27]. There are two modes of propagation (even and odd) of the coupled SPPs as shown in the figure below:

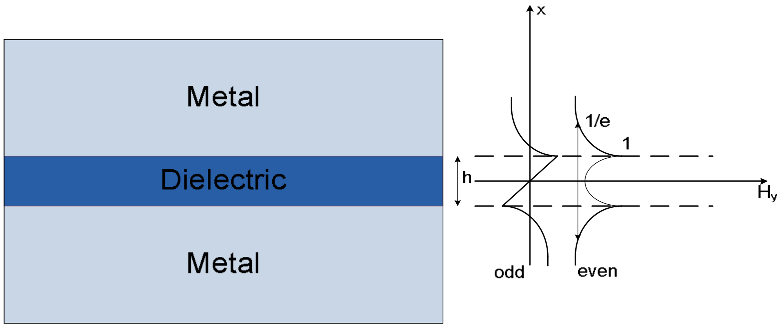

Fig.2-3 SPP at double interface

Chapter 3

Material Modeling

3.1 Material Dispersion

Material dispersion may be defined as the variation in wavelength of a propagating wave with change in frequency. It may also be defined as the variation of the wave number with angular frequency.

Due to material dispersion, when light travels through a given medium, the different wavelength components travel at different velocities. So if a pulse having a finite spectral bandwidth is launched in a dispersive material, the different wavelength components will travel at different velocities leading to a spread-out of the pulse in time and space. Though in theory, using a pulse having only one wavelength could overcome this problem, practically it is not realizable. Because any finite temporal pulse must have a finite frequency bandwidth due to the Fourier relation between the pulse duration and frequency bandwidth [28]. That is why in practical case such dispersion can never be avoided.

Since the response of materials to incident light heavily affects the properties of SPPs, in-depth study of the dispersive nature of materials supporting SPPs is needed.

Metals can be modeled as perfect conductors at frequencies lower than the optical range as no field is formed within metals for such frequencies. But at the optical range there exists field inside metals and hence they have to be modeled as dispersive materials. Though the fields die out very quickly inside metals within distances of the order of micrometers, this small distance is important for nanoscale devices. At frequencies higher than the optical range, metals behave as dielectrics.

The behavior of any material in response to as external oscillating electromagnetic field can be determined using three vectors – electric field intensity E, electric flux density D and polarization density P. These three vectors are interrelated as follows [29]:

$$D(\omega) = \varepsilon(\omega)E(\omega) \tag{3.1}$$

$$P(\omega) = \varepsilon_0\chi(\omega)E(\omega) \tag{3.2}$$

$$D(\omega) = \varepsilon_0 E(\omega) + P(\omega) \tag{3.3}$$

Using the expression of P from (3.2) into (3.3) we get

$$\mathrm{D}(\omega)=\varepsilon_0 E(\omega) + \chi(\omega)E(\omega) \tag{3.4}$$

$$\Rightarrow \mathrm{D}(\omega)=\varepsilon_0(1 + \chi(\omega))E(\omega) \tag{3.5}$$

Here χ represents the frequency dependent electric susceptibility of a material which indicates how easily it is polarized when an electric field is applied. This is a dimensionless quantity.

The relation between susceptibility and permittivity is

$$\varepsilon(\omega)=\varepsilon_0(1 + \chi(\omega)) \tag{3.6}$$

So, the relative permittivity is

$$\varepsilon_r(\omega) = 1 + \chi(\omega) \tag{3.7}$$

If the material is linear and isotropic (such as glass), these quantities have simple values but dispersive materials have frequency dependent permittivity and susceptibility which need to be modeled as accurately as possible to get the accurate response of the material when a certain electromagnetic excitation is applied. The mathematical models commonly used for this purpose are Debye model, Drude model. Lorentz model, Lorentz-Drude model, modified Lorentz model etc. Among them, we have used Drude model. Lorentz model, Lorentz-Drude model and modified Lorentz model in this thesis.

3.2 The Drude Model

Just after the discovery of electron in 1900, Paul Drude proposed a model for metal in which he described metal as a volume filled with stationary positive ions, immersed in a gas of electrons following the kinetic theory of gases. Due to the charge shielding effect these electrons can move freely inside the metal without any mutual interaction. The motion of these electrons is governed by the external electric force. The inter-ionic collisions act as the damping force for their motion [6, 30].

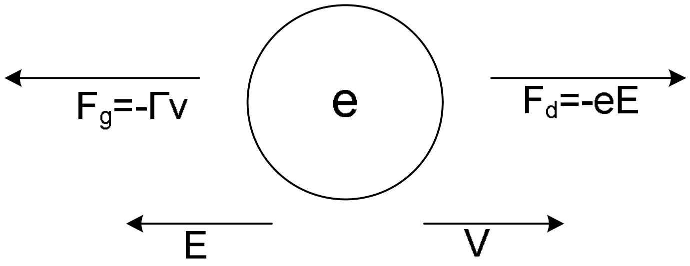

Figure 3-1: A free electron under the influecne of different forces in Drude model

In a metal an electron is subjected to two forces- the driving force F_d and the damping force F_g which are defined as follows:

$$F_d = qE = -eE \tag{3.8}$$

$$F_g = -\Gamma v \tag{3.9}$$

here, Γ is the damping constant and e is the charge of an electron. The resultant force is given by

$$F = F_d - F_g \tag{3.10}$$

Again from Newton's first law of motion we get

$$mr'' = -eE + \Gamma r' \tag{3.11}$$

here,

m is the mass of an electron.

r is the displacement.

Γ is the damping constant.

The number of primes indicate the order of differentiation with respect to time.

If the electric field and displacement are time harmonic, then

$$E(t) = E_0 e^{-j\omega t} \Leftrightarrow E(\omega) \qquad (3.12)$$

$$r(t) = R_0 e^{-j\omega t} \Leftrightarrow R(\omega) \qquad (3.13)$$

Now, the frequency domain form of equation (3.11) is

$$mR^n(\omega) - \Gamma m R'(\omega) + eE(\omega) = 0 \qquad (3.14)$$

$$\Rightarrow -m\omega^2 R(\omega) + j\omega m\Gamma R(\omega) + eE(\omega) = 0 \qquad (3.15)$$

$$\Rightarrow R(\omega)(j\omega m\Gamma - \ m\omega^2) = -eE(\omega) \qquad (3.16)$$

$$\Rightarrow R(\omega) = \frac{-e}{m(j\Gamma\omega - \omega^2)} E(\omega) \qquad (3.17)$$

For n number of electrons the polarization will be

$$P(\omega) = -neR(\omega) \qquad (3.18)$$

Using the expression of $R(\omega)$ from equation (3.17) into equation (3.18) we get,

$$P(\omega) = \frac{ne^2}{m(j\Gamma\omega - \omega^2)} E(\omega) \qquad (3.19)$$

$$\Rightarrow \frac{P(\omega)}{\varepsilon_0 E(\omega)} = \frac{ne^2}{\varepsilon_0 m(j\Gamma\omega - \omega^2)} = \chi(\omega) \qquad (3.20)$$

Substituting this expression of χ in equation (3.7) we get

$$\varepsilon(\omega) = 1 + \frac{ne^2}{\varepsilon_0 m(j\Gamma\omega - \omega^2)} \tag{3.21}$$

$$\Rightarrow \varepsilon(\omega) = (1 + \frac{\omega_p^2}{j\Gamma\omega - \omega^2}) \tag{3.22}$$

where $\omega_p^2 = \frac{ne^2}{\varepsilon_0 m}$.

here ω_p represents the plasma frequency.

Combining (3.22) and (3.1) we finally get the Drude model:

$$D(\omega) = \varepsilon_0 \left(1 + \frac{\omega_p^2}{j\Gamma\omega - \omega^2}\right) E(\omega) \tag{3.23}$$

Now, $\Gamma\omega << 1$ for low frequencies. So, we can write

$$D(\omega) = \varepsilon_0 \left(1 - \frac{\omega_p}{\omega^2}\right) E(\omega) \tag{3.24}$$

3.3 The Lorentz Model

Unlike the Drude model, electrons in the Lorentz model are not able to move freely inside the metal. Rather, the electrons are bound to atoms and hence a restoring force F_r acts on them. So, in the Lorentz model an electron can be considered to be bound to the nucleus through a spring as shown in the figure below:

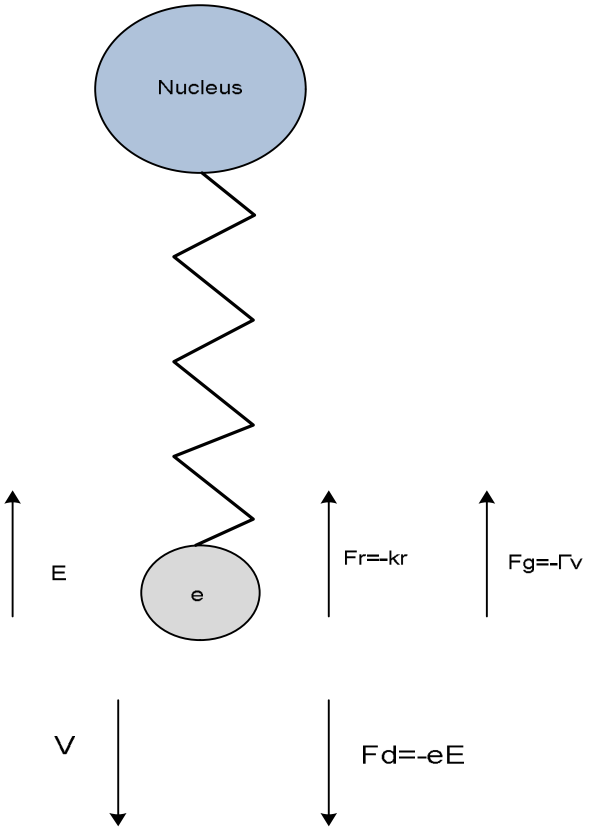

Figure 3-2: A free electron under the influence of different forces in Lorentz model

The restoring force is given by:

$$F_r = -kr \tag{3.25}$$

where k represents the spring constant.

So, from equation (3.11) we get

$$mr''m\Gamma r' + mkr + eE = 0 \tag{3.26}$$

Now, we can define $\sqrt{\frac{k}{m}}$ as the natural frequency ω_0.

Then following the same steps done for Drude model, we get

$$D(\omega) = \varepsilon_0\left(1 + \frac{\omega_p^2}{\omega_0^2 + j\Gamma\omega - \omega^2}\right)E(\omega) \tag{3.27}$$

Equation (3.27) represents the Lorentz model.

3.4 The Lorentz-Drude Model

In the Lorentz-Drude (LD) model, two different types of electron oscillations are considered- oscillation of free electrons and oscillation of bound electrons. The free electrons contribute to the Drude model permittivity and the bound electrons contribute to the Lorentz model permittivity. So, in this model,

$$\varepsilon = \varepsilon_{free} + \varepsilon_{bound} \tag{3.28}$$

$$\varepsilon_{free} = 1 + \frac{\omega_p}{j\Gamma\omega + \omega^2} \tag{3.29}$$

$$\varepsilon_{bound} = \frac{\omega_P}{\omega_0 + j\Gamma\omega + \omega^2} \tag{3.30}$$

Therefore, combining both the models, the electric field density D will be

$$D(\omega) = \varepsilon_0\left(1 + \frac{\omega_p}{j\Gamma\omega - \omega^2} + \frac{\omega_p}{\omega_0 + j\Gamma\omega - \omega^2}\right)E(\omega) \tag{3.31}$$

3.5 The Modified Lorentz Model

The modified Lorentz model is based on the generalized critical point models described as follows [11] :

$$\varepsilon(\omega) = \varepsilon_\infty + \sum_{p=1}^{p} \varepsilon_p(\omega) \tag{3.32}$$

$$\varepsilon_p(\omega) = \frac{a_{p,0} + a_{p,1}(-i\omega)}{b_{p,0} + b_{p,1}(-i\omega) - b_{p,2}\omega^2} \tag{3.33}$$

where ε_∞ is the permittivity at infinite frequency. The other quantities in (3.33) do not necessarily have any physical meaning.

Based on (3.32) and (3.33) the modified Lorentz model is defined as follows [11]:

$$\varepsilon(\omega) = \varepsilon_\infty + \sum_{n=1}^{N} \frac{\Delta\varepsilon_n(\omega_n^2 - j\omega\delta_n')}{\omega_n^2 - 2j\omega\delta_n - \omega^2} \tag{3.34}$$

Chapter 4

Finite-Difference Time-Domain Method

4.1 The Yee Algorithm

In order to solve Maxwell's time domain equations Yee recommended an algorithm for simulating wave propagations which is known as FDTD. Originally, Yee contemplated a lossless, homogenous and isotropic medium where he discretized the volume into several cells taking Cartesian coordinates into consideration. The foundation of this algorithm is to solve the electric and magnetic field in a well-known leap frog pattern varying with respect to time and space.

FDTD method initiates with Maxwell's two fundamental equations:

$$\frac{\partial H}{\partial t} = -\frac{1}{\mu} \nabla \times E \qquad (4.1)$$

$$\frac{\partial E}{\partial t} = \frac{1}{\varepsilon} \nabla \times H \qquad (4.2)$$

The E and H field used in this equation are actually three dimensional vectors so each of them can be translated into three coupled scalar first order differential equations. If we use curl operation to manipulate equation (4.1) and (4.2) we will get the six following equations in Cartesian coordinates which are varying with respect to both time and space

$$\frac{\partial H_x}{\partial t} = \frac{1}{\mu} \left(\frac{\partial E_y}{\partial z} - \frac{\partial E_z}{\partial y} \right) \qquad (4.3)$$

$$\frac{\partial H_y}{\partial t} = \frac{1}{\mu} (\frac{\partial E_z}{\partial x} - \frac{\partial E_x}{\partial z}) \qquad (4.4)$$

$$\frac{\partial H_z}{\partial t} = \frac{1}{\mu} (\frac{\partial E_x}{\partial y} - \frac{\partial E_y}{\partial x}) \qquad (4.5)$$

$$\frac{\partial E_x}{\partial t} = \frac{1}{\varepsilon} (\frac{\partial H_z}{\partial y} - \frac{\partial H_y}{\partial z} \qquad (4.6)$$

$$\frac{\partial E_y}{\partial t} = \frac{1}{\varepsilon}\left(\frac{\partial H_x}{\partial z} - \frac{\partial H_z}{\partial x}\right) \tag{4.7}$$

$$\frac{\partial E_z}{\partial t} = \frac{1}{\varepsilon}\left(\frac{\partial H_y}{\partial x} - \frac{\partial H_x}{\partial y}\right) \tag{4.8}$$

For translating the above equations into difference equation we need to discretize the equations with respect to both time and space. Yee considered a unit cell to discretize the space where the field components are arranged in such a way that the face centers are representing the components of magnetic field while the cell edges are representing the components of electric field. In this configuration every electric field component (E) is surrounded by four magnetic field component (H) and the other way around. According to Faraday's and Ampere's law, this develops a spatially coupled system with the circulation of corresponding field. The spatial grid of Yee is illustrated in the fig 4.1

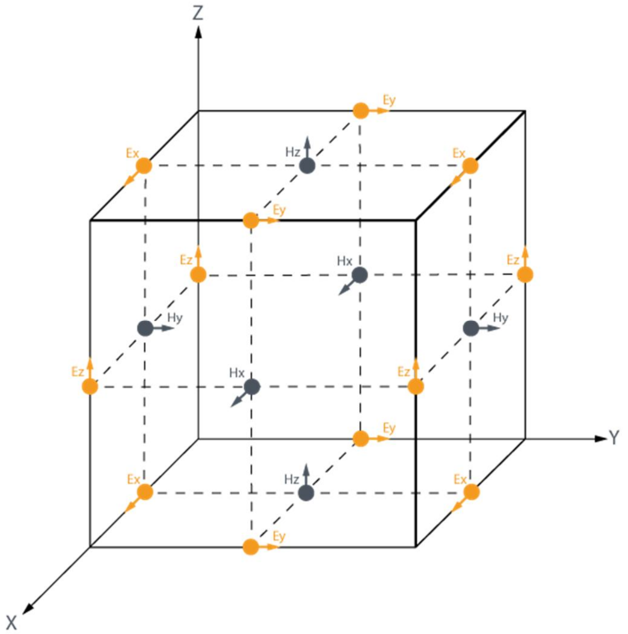

Figure 4.1: Yee's spatial grid.

Now in case of two dimensional polarized TM field we can write,

$$\frac{\partial E_x}{\partial t} = \frac{1}{\varepsilon}\frac{\partial H_z}{\partial y} \tag{4.9}$$

$$\frac{\partial E_y}{\partial t} = -\frac{1}{\varepsilon}\frac{\partial H_z}{\partial x} \qquad (4.10)$$

$$\frac{\partial H_z}{\partial t} = \frac{1}{\mu}\left(\frac{\partial E_x}{\partial y} - \frac{\partial E_y}{\partial x}\right) \qquad (4.11)$$

As we need to discretize the cell in space we need to discretize the above equations which yields,

$$\frac{\partial E_x}{\partial t} = \frac{1}{\varepsilon}\frac{H_z(i,j) - H_z(i,j-1)}{\Delta y} \qquad (4.12)$$

$$\frac{\partial E_y}{\partial t} = -\frac{1}{\varepsilon}\frac{H_z(i,j) - H_z(i-1,j)}{\Delta x} \qquad (4.13)$$

$$\frac{\partial H_z}{\partial t} = \frac{1}{\mu}\left(\frac{E_x(i,j+1) - E_x(i,j)}{\Delta y} - \frac{\partial E_y(i+1,j) - \partial E_y(i,j)}{\Delta x}\right) \qquad (4.14)$$

To implement the leap frog method we need to implement leap in time after the implementation of leap in space. Leap in time is the evaluation of electric field at an instant of time and using these values at a later instant of time we can calculate magnetic field which is illustrated in the fig 4.2

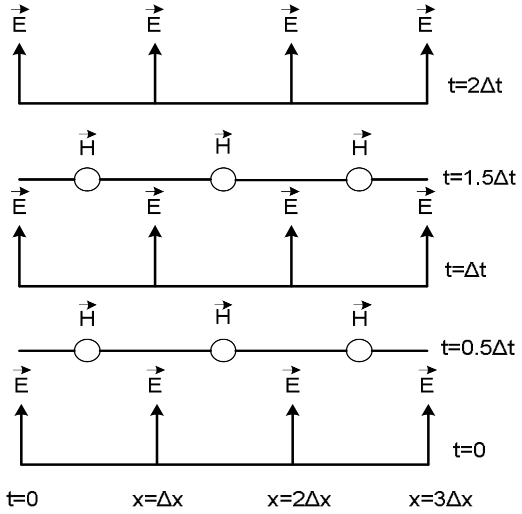

Figure 4.2: The temporal scheme of FDTD method.

Applying this method in (4.12), (4.13) and (4.14) we get,

$$\frac{E_x^n(i,j)-E_x^{n-1}(i,j)}{\Delta t} = \frac{1}{\varepsilon}\frac{H_z^{n-1/2}(i,j+1/2)-H_z^{n-\frac{1}{2}}(i,j-1/2)}{\Delta y} \tag{4.15}$$

$$\frac{E_y^n(i,j)-E_y^{n-1}(i,j)}{\Delta t} = -\frac{1}{\varepsilon}\frac{H_z^{n-1/2}(i+1/2,j)-H_z^{n-1/2}(i-1/2,j)}{\Delta x} \tag{4.16}$$

$$\frac{H_z^{n+\frac{1}{2}}(i,j)-H_z^{n-\frac{1}{2}}(i,j)}{\Delta t} = \frac{1}{\mu}\left(\frac{E_x^n\left(i,j+\frac{1}{2}\right)-E_x^n\left(i,j-\frac{1}{2}\right)}{\Delta y} - \frac{\partial E_y^n(i+1/2,j)-\partial E_y^n(i-1/2,j)}{\Delta x}\right) \tag{4.17}$$

Finally, if we update the equation (4.15), (4.16) and (4.17) with new values then the algorithm becomes

$$E_x^n(i,j) = E_x^{n-1}(i,j) + \frac{\Delta t}{\varepsilon}\frac{H_z^{n-1/2}(i,j+1/2)H_z^{n-1/2}(i,j-1/2)}{\Delta y} \tag{4.18}$$

$$E_y^n(i,j) = E_y^{n-1}(i,j) - \frac{\Delta t}{\varepsilon}\frac{H_z^{n-1/2}(i+1/2,j)H_z^{n-1/2}(i-1/2,j)}{\Delta x} \tag{4.19}$$

$$H_z^{n+1/2}(i,j) = H_z^{n-\frac{1}{2}}(i,j) + \frac{\Delta t}{\mu}\left(\frac{E_x^n(i,j+1/2)-E_x^n(i,j-1/2)}{\Delta y} - \frac{E_y^n(i+1/2,j)-E_y^n(i-1/2,j)}{\Delta x}\right) \tag{4.20}$$

As the simulation progresses the calculated components of electric and magnetic field will increase dramatically without any limit if the algorithm is unstable. So, in case of Yee algorithm it is required to ensure numerical stability which is done by limiting the phase velocity within the material to reduce the propagation speed of electro-magnetic field. By applying the criterion of Courant-Friedrichs-Lewy we can limit the time step Δt to ensure numerical stability for FDTD grid which is described by the equation

$$\Delta t \le \left\{\frac{1}{v_{p.}\sqrt{\frac{1}{(\Delta x)^2}+\frac{1}{(\Delta y)^2}+\frac{1}{(\Delta z)^2}}}\right\} \tag{4.21}$$

where Δx, Δy and Δz represents the increment of the spatial Cartesian grid.

4.2 Absorbing Boundary Condition (ABC)

As the computer memory resources are limited, it is not possible to simulate a theoretically infinite space in FDTD simulation. So, the simulation is done considering a finite cell for the computational simplicity. To implement it in the simulation, the cell boundary needs to be ideally absorbing so that there is no non-physical reflection of the propagated wave back to the cell region. The perfectly matched layer (PML), one of the best boundary conditions which was introduced by Berenger, is used in our simulation. The PML is actually an artificial layer surrounding the computational cell region which absorbs most of the outward waves. It prevents the reflection from the boundary through rapid attenuation of the EM field until they reduces to zero.

4.3 Material Dispersion in FDTD

The permittivity of a material is assumed to be constant which is not really correct. Actually, the permittivity and permeability of a material change with frequency causing dispersion in the material. This distortion hinders the realistic propagation of waves through the material creating the necessity of dispersive FDTD techniques. In order to analyze the material dispersion, the FDTD algorithm can be divided into three categories,

1. Auxiliary Differential Equation (ADE) which was introduced by Taflove.
2. The Z-Transform, introduced by Sullivans.
3. Recursive Convolution (RC) method, introduced by Luebbers.

We will try to discuss these three methods briefly in the following sections.

4.3.1 The Auxiliary Differential Equation (ADE)

In order to introduce the dispersion into the model Taflove proposed an ADE to the FDTD method. The main idea of this method is based on Fourier Transform by which the conversion of dispersion relation from the frequency domain to the time domain is done. A relationship between the new E field value and the previous E and D values is established through Fourier Transform. To update the E fields every time, this relation can be added to the algorithm and finally, the new algorithm with Auxiliary Differential Equation becomes

$$\frac{\partial H_z}{\partial t} = -\frac{1}{\mu}\left(\frac{\partial E_x}{\partial y} - \frac{\partial E_y}{\partial x}\right) \tag{4.22}$$

$$\frac{\partial D_x}{\partial t} = \frac{\partial H_z}{\partial y} \tag{4.23}$$

$$E = f(D, E) \tag{4.24}$$

To establish the function relation between D and E in a dispersive medium, we can start with the basic equation as follows

$$D(\omega) = \varepsilon_0 \frac{\sigma}{j\omega} E(\omega) \tag{4.25}$$

Multiplying the above equation with $j\omega$ we get

$$\mathrm{j\omega D(\omega) = \ \varepsilon_0 \sigma E(\omega)} \tag{4.26}$$

If we apply Fourier transform in (4.26) we will get

$$\frac{\partial D(t)}{\partial t} = \varepsilon_0 \sigma E(t) \tag{4.27}$$

Now, if we discretize the (4.27) by forward difference method, we can write

$$\frac{D^n - D^{n-1}}{\Delta t} = \varepsilon_0 \sigma E^n \tag{4.28}$$

Finally, solving for E, we can find the updated equation as

$$\varepsilon_0 \sigma E^n = \frac{D^n - D^{n-1}}{\Delta t} \tag{4.29}$$

$$\Rightarrow E^n = \frac{D^n - D^{n-1}}{\varepsilon_0\sigma\Delta t} \qquad (4\ 30)$$

4.3.2 The Z-Transform

To introduce the dispersion relation with FDTD algorithm, Sullivan initiated the use of Z-transform method. In comparison with Auxiliary Differential Equation method, the Z-transform method is faster.

The transformation between the frequency domain and the Z-domain is done as follows

$$D(\omega) = \varepsilon(\omega)E(\omega) \Leftrightarrow D(z) = \varepsilon(z)\Delta t E(z) \qquad (4.31)$$

where

$$\varepsilon(z) = \text{Z transform of } \varepsilon(\omega)$$

$$\Delta t = sampling\ period$$

To clear the idea, let us let us consider the material dispersion as $\frac{\sigma}{j\omega}$, same as we have done in ADE. The relation between D and E can be found from

$$D(\omega) = \varepsilon_0 \frac{\sigma}{j\omega} E(\omega) \qquad (4.32)$$

Applying the Z-transform we get

$$1 \quad z \qquad D(z) = \frac{\varepsilon_0\sigma}{- \quad ^{-1}} \Delta t E(z) \qquad (4.33)$$

Now, multiplying (4.24) by $(1 - z^{-1})$, we get

$$D(z)(1 - z^{-1}) = \varepsilon_0\sigma\Delta t E(z) \qquad (4.34)$$

$$\Rightarrow D(z) - z^{-1}D(z) = \varepsilon_0\sigma\Delta t E(z) \qquad (4.35)$$

Converting the Z-domain to the time domain by implementing inverse Z-transform, we get

$$D^n - D^{n-1} = \varepsilon_0\sigma\Delta t E^n \qquad (4.36)$$

Finally, solving (4.36) for E, we get,

$$E^n = \frac{D^n - D^{n-1}}{\varepsilon_0 \sigma \Delta t} \qquad (4.37)$$

This equation is same as the final updated equation of ADE method.

4.3.3 Recursive Convolution (RC) Method

The first frequency dispersive FDTD algorithm was formulated by Luebbers and to do this he used the Recursive Convolution (RC) method. After that it became piecewise linear recursive convolution (PLRC) [31] scheme. Though RC approach is not precise, it is faster than other approaches and utilizes less memory resources of the computer. But if we want to use multiple pole mediums, RC approach is easy to follow. For a linear dispersive medium, the derivation of piecewise linear recursive convolution (PLRC) method express the relation between electric flux density and electric field intensity, which is expressed as

$$D(t) = \varepsilon_0 \varepsilon_\infty E(t) + \varepsilon_0 \int_0^t E(t-\tau)\chi(\tau)d\tau \qquad (4.38)$$

The above equation can be discretized as:

$$D^n = \varepsilon_0 \varepsilon_\infty E^n + \varepsilon_0 \int_0^{n\Delta t} E(n\Delta t-\tau)\chi(\tau)d\tau \qquad (4.39)$$

From this basing discrete equation, the PRC method is further preceded.

4.3.4 The General Algorithm

The multi-pole dispersion relation equation derivation will be difficult in comparison with the single pole-pair dispersion relation. So, the required derivation process for six-pole Lorentz-Drude dispersion is lengthy. Moreover, the memory requirement for computation is also large. So, regarding this topic the researchers have proposed several methods such as Multi-term dispersion introduced by Okoniewski, Taflove's matrix inversion method etc. A general algorithm technique was proposed by Al-sunaidi and Al-Jabr by which they were able to solve various problems regarding previous methods. For any dispersion relation, this method requires only one algorithm which is the key advantage of this technique. The general form of dispersion relation is,

$$D(\omega) = \varepsilon(\omega)E(\omega) \qquad (4.40)$$

This equation can be expressed in terms of summation of poles as follows,

$$D(\omega) = \varepsilon_0 \varepsilon_\infty E(\omega) + \sum_i^N P_i(\omega) \qquad (4.41)$$

where N is the number of the poles.

Applying Fourier transform in the above equation, we get

$$D^{n+1} = \varepsilon_0 \varepsilon_\infty E^{n+1} + \sum_i^N P_i^{n+1} \qquad (4.42)$$

$$\Longrightarrow E^{n+1} = \frac{D^{n+1} - \sum_i^N P_i^{n+1}}{\varepsilon_0 \varepsilon_\infty} \qquad (4.43)$$

where term P_i can be any form of dispersion relation such as the Debye, the Drude or just the conductivity term.

The equation 4.43 is the final solve equation for E.

Chapter 5

Extraction of parameters for material modeling

5.1 Introduction

The original FDTD formulations provided by Yee ignores the dispersive nature of materials. For practical materials this idealization is either invalid or valid only for a narrow range of wavelength. So if the wavelength range of interest is not narrow then the whole range has to be divided into many narrow subranges such that the idealization can be applied to each subrange. Then FDTD simulation has to be performed for each subrange separately and the results have to be combined together to get the solution for the whole wavelength range. As a result the simulation will be computationally inefficient and time consuming. So, for a computationally efficient algorithm, the variation of complex dielectric permittivity of the used materials over long wavelength range must be incorporated.

Experimental values of this variation for different materials have been determined by different researchers. But the experimental data of variation of complex permittivity functions cannot be substituted directly in tabular form into the FDTD algorithm due to its inherent structure. Instead, an approximate mathematical model of the variation of permittivity with frequency has to be used in FDTD [32].

In chapter 3 we discussed about different mathematical models to approximate the frequency dependent permittivity of materials. Before performing FDTD simulation of any material, it needs to be characterized using any one of these mathematical models i.e. the parameters describing that model for that particular material are to be found out and optimized to match the experimental permittivity as much as possible.

In this thesis we have used an algorithm based on the Nelder Mead method [33] to extract different model parameters for 15 materials- cadmium indium telluride ($CdIn_2Te_4$), cupric oxide (CuO), hafnium nitride (HfN), liquid mercury (Hg), indium phosphide (InP), mercury cadmium telluride ($Hg_{1-x}Cd_xTe$; x=0.2), molybdenum (Mo), osmium (Os), lead sulphide (PbS), lead selenide (PbSe), rhodium (Rh), tantalum (Ta), thulium (Tm), titanium nitride (TiN) and zirconium nitride (ZrN).

The experimental data of frequency dependent permittivity of these materials are taken from [34-38]. The complex relative permittivity of each of these materials has been calculated using the obtained parameters to compare the optimized permittivity curve with the experimental one. It is observed that the calculated permittivities are in very good agreement with the experimental data. Besides, we have compared the performances of different mathematical models used for each material.

5.2 Mathematical Models Used

The wavelength dependency of the complex dielectric function of a material can be approximated using the Lorentz oscillator model given by [25]:

$$\varepsilon(\omega) = \varepsilon_\infty + \sum_{n=1}^{N_L} \frac{\Delta\varepsilon_n \omega_n^2}{\omega_n^2 + 2j\omega\delta_n - \omega^2} \tag{5.1}$$

where ε_∞ is the relative permittivity at infinite frequency, N_L represents the total number of Lorentz pole pairs used for modeling, the change in relative permittivity of the material for the N^{th} pole pair is represented by $\Delta\varepsilon_n$, ω_n is the undamped frequency of the N^{th} pole pair and δ_n is the corresponding damping factor.

The Lorentz-Drude model is given by [32]:

$$\varepsilon(\omega) = \varepsilon_\infty - \sum_{n=1}^{N_{D(LD)}} \frac{\Delta\varepsilon_n \omega_n^2}{j\omega\delta_n + \omega^2} \quad + \sum_{n=1}^{N_{L(LD)}} \frac{\Delta\varepsilon_n \omega_n^2}{\omega_n^2 - 2j\omega\delta_n - \omega^2} \tag{5.2}$$

The Drude model is given by [32]:

$$\varepsilon(\omega) = \varepsilon_\infty - \sum_{n=1}^{N_D} \frac{\Delta\varepsilon_n \omega_n^2}{j\omega\delta_n + \omega^2} \tag{5.3}$$

The modified Lorentz model is given by [11]:

$$\varepsilon(\omega) = \varepsilon_\infty + \sum_{n=1}^{N_{ML}} \frac{\Delta\varepsilon_n (\omega_n^2 - j\omega\delta_n')}{\omega_n^2 - 2j\omega\delta_n - \omega^2} \tag{5.4}$$

In the above equations, N represents the number of pole pairs used and the associated subscripts indicate the name of the model; L, ML, D and LD stand for Lorentz, modified Lorentz, Drude and lorentz-Drude respectively.

5.3 Optimization Method

A nonlinear optimization algorithm for extracting the Lorentz model parameters of the mentioned materials has been developed based on the Nelder Mead method [33].

The Nelder Mead method can be programmed easily, requires little storage, deals with a set of points instead of a single point and does not require any derivative information. Because of these advantages, this technique has been applied for optimization purpose in different fields. For example, the HEC-HMS 2000, a software developed by the U.S. Army Corps of Engineers uses this method for hydrological modeling [39].

The algorithm takes the experimental values of real (ε_{rex}) and imaginary (ε_{iex}) parts of complex permittivity of the material, a set of starting values of the parameters and a tolerance level for error as input.

If the refractive index (n) and extinction co-efficient (k) are supplied as input, then it can calculate ε_{rex} and ε_{iex} using the following relations [38]:

$$\varepsilon_{rex} = n^2 - k^2$$

$$\varepsilon_{iex} = 2nk$$

Using the provided inputs, the algorithm calculates the complex relative permittivity of the material using the Lorentz model and compares it with the experimental data. An objective function is used to calculate the amount of mismatch between the experimental and modeled data.

The following objective function was found to work well for Lorentz modeling of dispersive materials using Nelder Mead method:

$$f = \sqrt{\sum(x_1^2 + x_2^2)}$$

where

$$x_1 = \varepsilon_{rc} - \varepsilon_{rex}$$

$$x_2 = \varepsilon_{ic} - \varepsilon_{iex}$$

Where ε_{rc} is the modeled real part of permittivity, ε_{rex} is the experimental value of real part of permittivity, ε_{ic} is the modeled imaginary part of permittivity, ε_{iex} is the experimental value of imaginary part of permittivity.

If the error is within the tolerance level, then the starting values are given as output. Otherwise, the algorithm advances iteratively to minimize the objective function till the error comes down to the tolerance level.

The algorithm uses the Nelder-Mead method for minimizing the objective function. Like genetic algorithms, it advances iteratively by modifying a group of possible solutions till they converge to a single optimal solution. The method involves 5 major steps- initialization, reflection, expansion, contraction and shrinking [33].

At the **initialization** step, for minimizing a function of k variables, a simplex with $k+1$ number of vertices is defined. Then the function is evaluated at each vertex of the simplex.

At the **reflection** step, the stopping criterion is checked first. If the criterion is not fulfilled, then the vertices for which the function has the maximum (y_{max1}), second maximum (y_{max2}) and minimum (y_{min}) values are identified. Let those vertices are x_{max1}, x_{max2} and x_{min} respectively. The vertex x_{max1} is then reflected through the centroid x_{cen} of the other vertices in order to get a new vertex x_{ref}. The vertex x_{ref} is obtained using the following equation:

$$x_{ref} = (1 + \alpha)x_{cen} - \alpha x_{max1}$$

where α =1 is the reflection coefficient.

Then the function is evaluated at the vertex x_{ref} and let the value be denoted by y_{ref} . The vertex x_{max1} is replaced by x_{ref} if $y_{min} \le y_{ref} \le y_{max2}$ and the reflection process is repeated.

Now if $y_{ref} < y_{min}$, then the reflection is **expanded** in the same direction, thus expanding the search region. The expansion is done using the following equation:

$$x_{exp} = \gamma x_{ref} + (1 - \gamma)x_{cen}$$

where γ=2 is the expansion coefficient.

The new vertex (x_{exp}) obtained by expansion will replace x_{max1} if y_{exp}<y_{min}. Otherwise x_{max1} is replaced by x_{ref} and the algorithm performs a new iteration of the reflection step.

In the next step, if $y_{max2} < y_{ref} \leq y_{max1}$, then x_{max1} is replaced by x_{ref} and **contraction** is performed. If y_{ref}>y_{max1}, then the direct contraction is performed without replacing x_{max1} by x_{ref}. The contraction vertex x_{con} is obtained by the following equation:

$$x_{con} = \beta x_{max1} + (1 - \beta)x_{cen}$$

where β=0.5 is the contraction coefficient.

The vertex x_{max1} is replaced by x_{con} if $y_{con} \leq y_{max1}$. Then a fresh iteration begins from the reflection step.

The contraction is considered to have failed if $y_{con} > y_{max1}$. Then the entire simplex except x_{min} is **shrinked** by

$$x_i \longleftarrow \delta x_i + (1 - \delta)x_{min}, i \neq min$$

Then the function value is evaluated at each vertex except x_{min} and a new iteration is performed from the reflection step. Every time the algorithm performs the reflection step, a stopping criterion is calculated as follows:

$$\sum_{i=1}^{k+1} \frac{(y_i - \bar{y})^2}{k + 1} \leq \theta$$

where θ is the predefined tolerance.

The whole process is summarized in the following flow-chart:

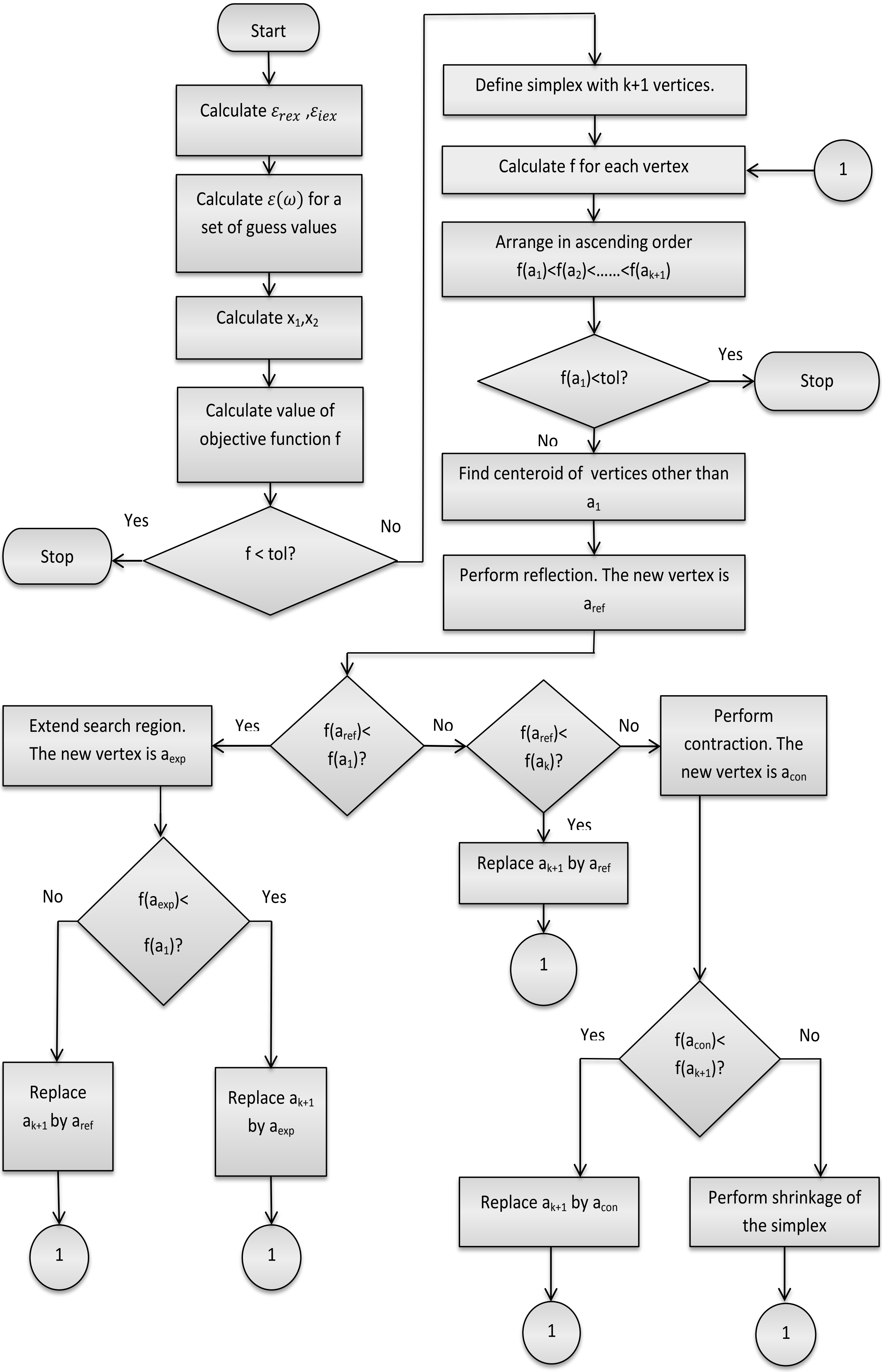

Fig.1. The flowchart of the optimization algorithm based on Nelder Mead method

5.4 The Optimized Parameters

The optimized parameters are presented in TABLE 1. The real and imaginary parts of the complex relative permittivity of the materials are plotted for both modeled and experimental data and are shown in FIG. 5-2 upto FIG 5-16.

From TABLE 1,2,3,4 it observed that the RMS deviations are very small. Besides, very good agreement is found between the experimental and modeled curves for all the materials.

Since the modeled parameters are applicable for long wavelength ranges, FDTD simulation involving these materials can provide broadband results in single simulation instead of dividing the wavelength range of interest into small portions and running the simulation for each portion separately. As a result, the simulation will be less time consuming.

The different modeling parameters of the materials are presented in Table 1-4.

TABLE 1. THE OPTIMIZED LORENTZ MODEL PARAMETERS

Parameters	Materials														
	$CdIn_2Te_4$	CuO	HfN	Hg	InP	HgCdTe	Mo	Os	PbS	PbSe	Rh	Ta	Tm	TiN	ZrN
ε_∞	42.5798	2.6459	5.0868	1.1	1.5173	1.4	794.4534	14.95	1.1	1	2	13.0488	1.6393	1.1	1.1
$\Delta\varepsilon_1$	0.7352	6.0492	1111	1.0678×10^{3}	4.8703	1.355	-196.0252	768.4683	-1.684	0.6507	-29.8	889.8663	-54.3341	-148.9153	1111
$\Delta\varepsilon_2$	14.5114	0.2198	42.27	-59.1412	1.4047	0.9333	-313.1677	-238.947	0.0552	0.0892	13.71	-15.5017	-19.1435	-515.0224	2.9441
$\Delta\varepsilon_3$	-48.6552	-6.7	--------	--------	1.2563	7.1008	-778.3790	-891.821	8.5341	3.2623	-206.96	--------	-0.1444	-0.4767	--------
$\Delta\varepsilon_4$	--------	4.4471	--------	--------	1.2096	0.6358	--------	--------	2.274	2.3388	--------	--------	--------	--------	--------
$\Delta\varepsilon_5$	--------	--------	--------	--------	--------	--------	--------	--------	3.3747	8.6195	--------	--------	--------	--------	--------
$\Delta\varepsilon_6$	--------	--------	--------	--------	--------	--------	--------	--------	--------	9.4656	--------	--------	--------	--------	--------
δ_1 (rad/sec)	-4.769×10^{14}	-7.24×10^{14}	-1.55×10^{14}	-3.04×10^{19}	-2.1×10^{15}	-6.41×10^{14}	-2.65×10^{15}	-2.2×10^{21}	-3.74×10^{15}	-3×10^{18}	-1.16×10^{16}	-5.65×10^{13}	1.43×10^{19}	-1×10^{16}	-2.26×10^{14}
δ_2 (rad/sec)	-1.962×10^{15}	4.2×10^{14}	-7.62×10^{14}	-3.41×10^{16}	-8.14×10^{14}	-3.26×10^{14}	-2.39×10^{16}	8.1336×10^{15}	1.83×10^{14}	-1.81×10^{18}	3.77×10^{12}	1.63×10^{18}	-2.42×10^{19}	3.63×10^{16}	-2.47×10^{15}
δ_3 (rad/sec)	-2.146×10^{21}	-7.6×10^{14}	--------	--------	-2.99×10^{14}	-4.42×10^{15}	7.63×10^{14}	-2.244×10^{19}	-1.04×10^{15}	-7.28×10^{14}	8.52×10^{18}	--------	-2.24×10^{14}	6.54×10^{14}	--------
δ_4 (rad/sec)	--------	-3.3×10^{15}	--------	--------	3.34×10^{14}	-6.8×10^{14}	--------	--------	-6.56×10^{14}	-4.05×10^{14}	--------	--------	--------	--------	--------
δ_5 (rad/sec)	--------	--------	--------	--------	--------	--------	--------	--------	-1.63×10^{18}	-7.58×10^{14}	--------	--------	--------	--------	--------
δ_6(rad/sec)	--------	--------	--------	--------	--------	--------	--------	--------	--------	-3.43×10^{16}	--------	--------	--------	--------	--------
ω_1(rad/sec)	3.8265×10^{15}	2.71×10^{15}	2.79×10^{14}	9.4×10^{16}	7.64×10^{15}	4.4×10^{15}	1.81×10^{15}	1.692×10^{18}	2.85×10^{16}	1.20×10^{15}	8.99×10^{15}	3.39×10^{14}	1.07×10^{17}	3.84×10^{15}	3.28×10^{14}
ω_2(rad/sec)	6.1619×10^{15}	2.99×10^{15}	1.052×10^{15}	1.34×10^{16}	5.41×101^{5}	3.5×10^{15}	-4.87×10^{15}	2.5862×10^{15}	4.27×10^{15}	7.95×10^{14}	9.26×10^{14}	7.19×10^{16}	1.66×10^{17}	4.08×10^{15}	9.51×10^{15}
ω_3(rad/sec)	1.2369×10^{19}	2.63×10^{15}	--------	--------	4.84×10^{15}	7.4×10^{15}	1.78×10^{16}	1.7079×10^{17}	4.78×10^{15}	3.53×10^{15}	1.05×10^{17}	--------	5.05×10^{15}	5.37×10^{15}	--------
ω_4(rad/sec)	--------	6.3×10^{15}	--------	--------	7.18×10^{15}	7.1×10^{15}	--------	--------	2.93×10^{15}	2.45×10^{15}	--------	--------	--------	--------	--------
ω_5(rad/sec)	--------	--------	--------	--------	--------	--------	--------	--------	1.5×10^{17}	4.16×10^{15}	--------	--------	--------	--------	--------
ω_6(rad/sec)	--------	--------	--------	--------	--------	--------	--------	--------	--------	1.29×10^{16}	--------	--------	--------	--------	--------
Range of wavelength (nanometer)	450-1000	300-1000	300-2000	200-1550	250-850	200-850	600-2000	800-2000	200-2000	300-1100	400-1770	600-2000	400-1050	350-1900	200-1800
RMS Deviation	0.0796	0.1592	0.6924	0.754	0.2118	0.0672	1.1943	0.6485	0.3713	0.6107	1.9	0.3884	0.1049	0.4682	1.0890

TABLE 2. THE OPTIMIZED LORENTZ-DRUDE MODEL PARAMETERS

Parameters	Materials							
	$CdIn_2Te_4$	CuO	HfN	Hg	InP	Mo	Os	Ta
ε_∞	2.7954	1	4.4400	1	2.9600	14	1	8.2500
$\Delta\varepsilon_{1L}$	0.8646	-45.9516	-225.2823	-46.6367	6.0584	8.7053	122.0783	14.2369
$\Delta\varepsilon_{2L}$	5.8702	22.4568	-----	-----	1.7242	1.7242	16.1026	-----
$\Delta\varepsilon_{3L}$	-----	29.8761	-----	-----	-----	-----	96.3964	-----
$\Delta\varepsilon_{4L}$	-----	0.5917	-----	-----	-----	-----	-1.2927	-----
$\Delta\varepsilon_{1D}$	-9.4738	49.9468	21.5000	6.2000	-1.1481	0.1199	8.9000e-05	8.0500e-04
ω_{1L}(rad/sec)	3.8283e+15	3.3848e+16	-2.0441e+17	-9.7509e+15	7.1760e+15	2.9537e+15	-1.0094e+16	-7.0307e+17
ω_{2L}(rad/sec)	5.3627e+15	4.2104e+16	-----	-----	4.8839e+15	-8.7630e+16	6.4334e+15	-----
ω_{3L}(rad/sec)	-----	9.5473e+15	-----	-----	-----	-----	3.5475e+16	-----
ω_{4L}(rad/sec)	-----	2.9801e+15	-----	-----	-----	-----	2.2337e+15	-----
ω_{1D}(rad/sec)	1.2947e+17	9.4957e+16	2.0472e+17	7.7355e+16	9.1873e+15	2.8976e+16	9.0999e+17	4.0725e+17
δ_{1L}(rad/sec)	4.9763e+14	3.0569e+17	2.7945e+19	1.5811e+16	1.9585e+15	7.6718e+14	7.8053e+17	1.3941e+20
δ_{2L}(rad/sec)	1.2064e+15	-9.3826e+17	0	0	3.1479e+14	-4.7817e+18	2.1243e+15	0
δ_{3L}(rad/sec)	-----	1.3114e+16	0	0	0	0	3.8533e+18	0
δ_{4L}(rad/sec)	-----	5.9188e+14	5.9188e+14	5.91887e+14	5.9188e+14	5.9188e+14	5.9188e+14	5.91880e+14
δ_{1D}(rad/sec)	1.5421e+20	1.2824e+19	5.3321e+18	2.6214e+17	5.3648e+17	3.7699e+13	3.7699e+13	3.7699e+13
Range of wavelength (nanometer)	450-1000	350-1000	300-2000	200-1040	400-830	615-2000	670-1770	620-1590
RMS Deviation	0.0600	0.2600	1.2551	0.7763	0.0930	0.6617	0.5403	0.6261

TABLE 3. THE OPTIMIZED MODIFIED LORENTZ MODEL PARAMETERS

Parameters	Materials												
	$CdIn_2Te_4$	CuO	HfN	Hg	InP	HgCdTe	Mo	PbS	PbSe	Ta	Tm	TiN	ZrN
ε_∞	1	12.2870	1000	997.6000	1	1	4.9593e+003	1.5295	5.0863	1.0277e+3	160.2477	25.5800	4.7608e+3
$\Delta\varepsilon_1$	6.2772	0.0001	-13.3005	79.8501	7.2670	9.4164	-0.5659	-0.0011	12.1288	-16.0281	17.6244	-0.5109	-33.3034
$\Delta\varepsilon_2$	1.8452	-5.5731	96.5178	-20.7504	2.9816	1.9314	-94.6059	0.1042	10.7616	-97.8544	-10.9229	99.9973	-19.3648
$\Delta\varepsilon_3$	-----	-----	-8.1720	-----	-----	-----	-25.6043	0.0033	-0.3004	-0.0084	0.0446	-0.0508	-68.5474
$\Delta\varepsilon_4$	-----	-----	-----	-----	-----	-----	52.7430	16.0136	-0.0064	99.9999	-0.2009	97.3844	-----
ω_1(rad/sec)	6.2090e+15	2.6069e+15	2.4640e+16	1.4637e+16	3.0219e+17	2.0414e+17	-0.0656e+16	3.3778e+15	4.0828e+15	6.7655e+16	4.3955e+16	1.1696e+16	0.0162e+16
ω_2(rad/sec)	3.7963e+15	9.3343e+15	0.6186e+16	-0.9749e+16	-0.0499e+17	-0.0351e+17	3.2489e+16	6.6595e+15	2.4561e+15	0.1583e+16	8.5108e+16	-7.5430e+16	0.1382e+16
ω_3(rad/sec)	-----	-----	0.6288e+16	-----	-----	-----	0.1762e+16	6.8857e+15	-7.8301e+15	-0.0558e+16	1.6341e+16	-0.0888e+16	9.5488e+16
ω_4(rad/sec)	-----	-----	-----	-----	-----	-----	1.5619e+16	4.8556e+15	9.9469e+15	0.6426e+16	0.2925e+16	1.7803e+16	-----
δ_1(rad/sec)	2.0678e+15	5.3910e+14	5.9663e+16	0.3546e+17	3.3763e+18	3.8536e+18	0.0181e+17	0.6202e+15	0.8595e+15	3.4308e+17	1.5859e+18	0.0957e+18	0.0020e+17
δ_2(rad/sec)	0.8162e+15	1.0000e+14	4.2903e+16	3.5026e+17	0.0004e+18	0.0005e+18	1.4393e+17	0.3921e+15	1.2139e+15	0.0321e+17	0.0552e+18	4.6144e+18	0.1208e+17
δ_3(rad/sec)	-----	-----	8.7632e+16	-----	-----	-----	0.0230e+17	1.4363e+15	0.7012e+15	0.0027e+17	0	0.0005e+18	1.8418e+17
δ_4(rad/sec)	-----	-----	-----	-----	-----	-----	2.7901e+17	1.4175e+15	1.6324e+15	0.4633e+17	0.0194e+18	0.0011e+18	-----
δ'_1(rad/sec)	0.8954e+15	3.3116e+19	1.0000e+14	0.0118e+19	2.0000e+14	0	4.7124e+19	6.5045e+18	0e+18	4.6760e+19	1.7884e+19	4.6505 e+19	0.0011e+19
δ'_2(rad/sec)	2.7652e+15	0.0008e+19	0.1009e+19	3.8187+19	1.0000e+14	1.3421e+15	2.8831e+19	0e+18	0e+18	0.0059e+19	0.8331e+19	0.0085 e+19	0.5817e+19
δ'_3(rad/sec)	-----	-----	4.5649e+19	-----	-----	-----	0.0189e+19	4.7882e+18	0.0032e+18	4.4213e+19	3.2348e+19	0.2782 e+19	2.6150e+19
δ'_4(rad/sec)	-----	-----	-----	-----	-----	-----	4.7081e+19	0e+18	4.3755e+18	0	4.7065e+19	7.5398e+12	
Range of wavelength (nanometer)	250-992	350-1000	300-1800	200-1550	400-830	530-830	770-2000	200-2000	300-780	620-1590	500-1050	400-1130	410-1780
RMS Deviation	0.1153	0.3082	1.4604	0.5548	0.0706	0.1187	2.0730	0.4189	0.3323	0.7423	0.0810	0.3090	0.5631

TABLE 4. THE OPTIMIZED DRUDE MODEL PARAMETERS

Parameters	Materials						
	HfN	Hg	Mo	Os	Rh	Ta	Tm
ε_∞	4.5900	3.2300	1	15.0500	1	11.7700	1.3280
$\Delta\varepsilon_1$	10.0509	0.0146	0.0352	-0.6879	0.0054	3.4908	0.0812
$\Delta\varepsilon_2$	-----	-----	-0.0077	7.2322	0.000156	4.8300	98.2704
$\Delta\varepsilon_3$	-----	-----	0.4328	50.0395	-----	0.3006	19.2466
$\Delta\varepsilon_4$	-----	-----	-----	-----	-----	-----	2.5531
ω_1(rad/sec)	3.5795×10^{15}	1.6478×10^{17}	6.0861×10^{16}	4.9563×10^{17}	1.4625×10^{17}	5.9489×10^{15}	1.2955×10^{16}
ω_2(rad/sec)	-----	-----	6.1920×10^{17}	2.8348×10^{17}	1.9195×10^{18}	9.9332×10^{17}	9.5151×10^{16}
ω_3(rad/sec)	-----	-----	1.0077×10^{17}	1.1951×10^{15}	-----	5.3042×10^{17}	2.1257×10^{17}
ω_4(rad/sec)	-----	-----	-----	-----	-----	-----	7.2980×10^{16}
δ_1(rad/sec)	7.8037×10^{14}	2.6653×10^{15}	1.0933×10^{14}	2.9676×10^{17}	0	2.2619×10^{13}	2.6389×10^{13}
δ_2(rad/sec)	-----	-----	5.1346×10^{15}	9.8081×10^{17}	5.7265×10^{15}	5.3307×10^{20}	2.9409×10^{20}
δ_3(rad/sec)	-----	-----	7.6115×10^{15}	1.2441×10^{14}	-----	1.0420×10^{19}	1.3189×10^{20}
δ_4(rad/sec)	-----	-----	-----	-----	-----	-----	1.2245×10^{19}
Range of wavelength (nanometer)	200-2000	200-1040	820-2000	850-1910	400-1770	600-2000	500-1050
RMS Deviation	1.1266	0.5724	1.7307	0.7470	2.6613	0.7874	0.1045

5.5 Discussion on the Extracted Parameters

We present a comparison among the different models used for each material based on the following facts:

a) If the number of pole pairs used for modeling is less, then the FDTD algorithm that uses the model will be faster.

b) The wavelength range over which the modeling is applicable is the range over which the results of the FDTD simulation is valid. So, the wavelength range should be as long as possible.

c) The absolute deviations for different models have been calculated for each material as follows:

$$\text{Absolute deviation (at a particular wavelength)} \\ = \sqrt{(\text{error in real part at that wavelength})^2 + (\text{error in imaginary part at that wavelength})^2}$$

The absolute deviations at different wavelengths for all the models used for a particular material are divided by the maximum among them to get the values of normalized absolute deviations at different wavelengths.

A lower trajectory of the normalized absolute deviation curve indicates better accuracy.

Cadmium indium telluride:

Cadmium indium telluride has been modeled using Lorentz, modified Lorentz and Lorentz-Drude models. FIG. 5-2 shows that for all the models, the optimized permittivity curves have very good agreement with the experimental curves.

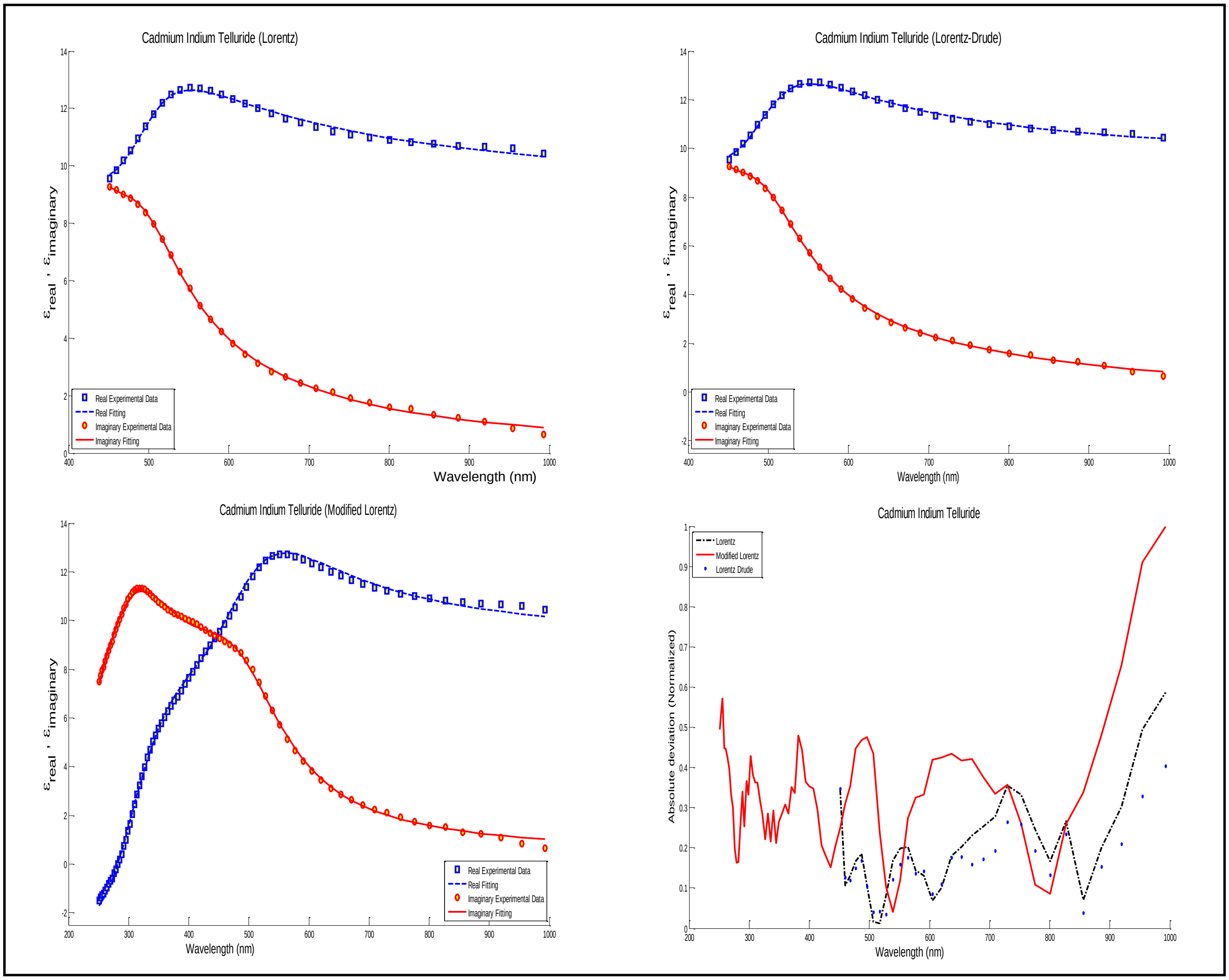

FIG. 5-2 Comparison between modeled and experimental complex permittivities of cadmium indium telluride

The number of pole pairs used for Lorentz and modified Lorentz models are 3 and 2 respectively. For the Lorentz-Drude model, we used 1 Drude term and 2 Lorentz terms. Increasing the number of pole pairs beyond these values did not improve the fitting significantly.

The optimization performed using the modified Lorentz model covers the longest wavelength range (250-1000 nm) among the three models used. But the normalized absolute deviation is the highest in this case.

The wavelength ranges for Lorentz and Lorentz-drude models are equal (450-1000 nm). But the normalized absolute deviation is the least for Lorentz-Drude model.

But if the wavelength range of 250-450 nm is within the range of interest, then the modified Lorentz model should be used.

Cupric oxide :

Lorentz, modified Lorentz and Lorentz-Drude models have been used to model the frequency dependent permittivity of cupric oxide . FIG.5-3shows that for all the models, the optimized permittivity curves have very good agreement with the experimental curves.

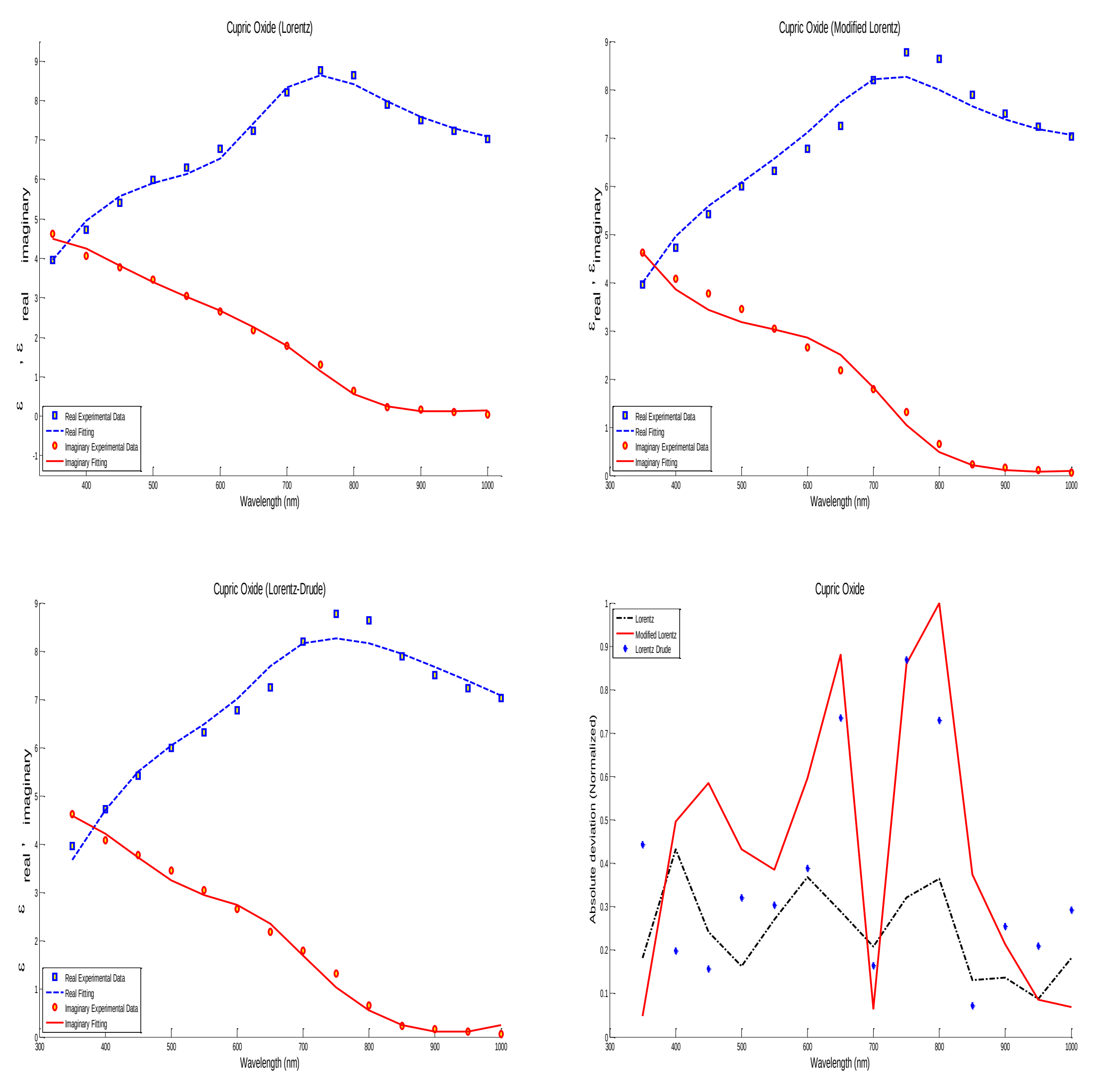

FIG. 5-3 Comparison between modeled and experimental complex permittivities of cupric oxide

The number of pole pairs used for Lorentz and modified Lorentz models are 4 and 2 respectively. For the Lorentz-Drude model, we used 1 Drude term and 4 Lorentz terms.

For all the three models, the wavelength range over which the modeling is applicable is 350-1000 nm. The normalized absolute deviation curve for the modified Lorentz model lies above the curves for the other two models for most parts of the wavelength range.

So, the data provided for either Lorentz or Lorentz-Drude model should be used for better accuracy in FDTD simulation of cupric oxide .

Hafnium nitride :

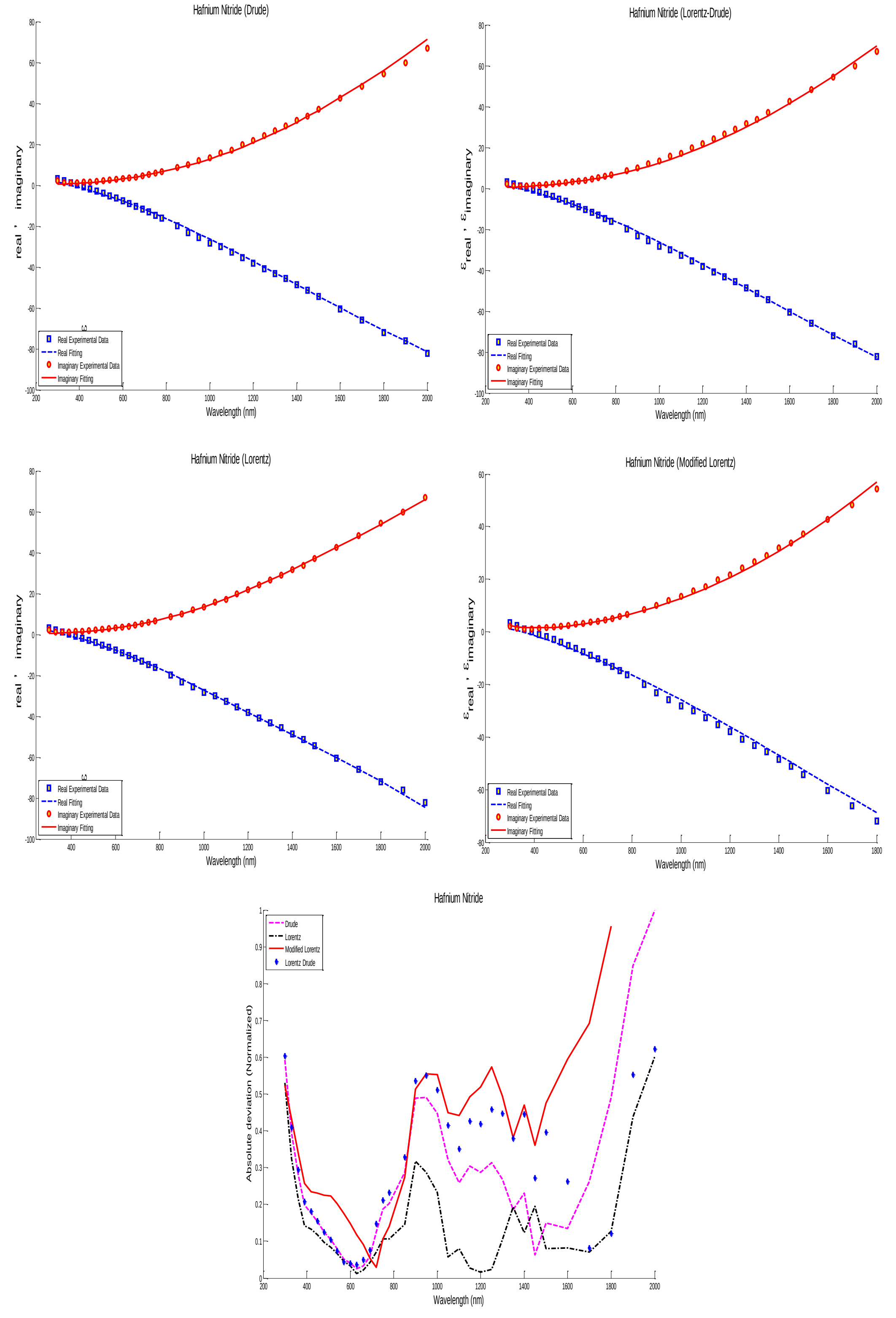

FIG.5-4 Comparison between modeled and experimental complex permittivities of hafnium nitride

Hafnium nitride has been modeled using Lorentz, modified Lorentz, Drude and Lorentz-Drude models. FIG.5-4 shows that for all the models, the optimized permittivity curves have very good agreement with the experimental curves.

The number of pole pairs used for Lorentz, modified Lorentz and Drude model are 2, 3 and 1 respectively. For the Lorentz-Drude model, we used 1 Drude term and 1 Lorentz term.

The fitting is applicable over wavelength ranges of 350-2000 nm for Lorentz model, 300-1800 nm for modified Lorentz model, 300-2000 nm for both Drude and Lorentz-Drude models.

From the normalized absolute deviation curves we see that the Lorentz fitting is the most accurate among the 4 models used for HfN.

Liquid mercury:

The modeling for liquid mercury has been performed using Lorentz, modified Lorentz, Drude and Lorentz-Drude models. FIG.5-5 shows that for all the models, the optimized permittivity curves have very good agreement with the experimental curves.

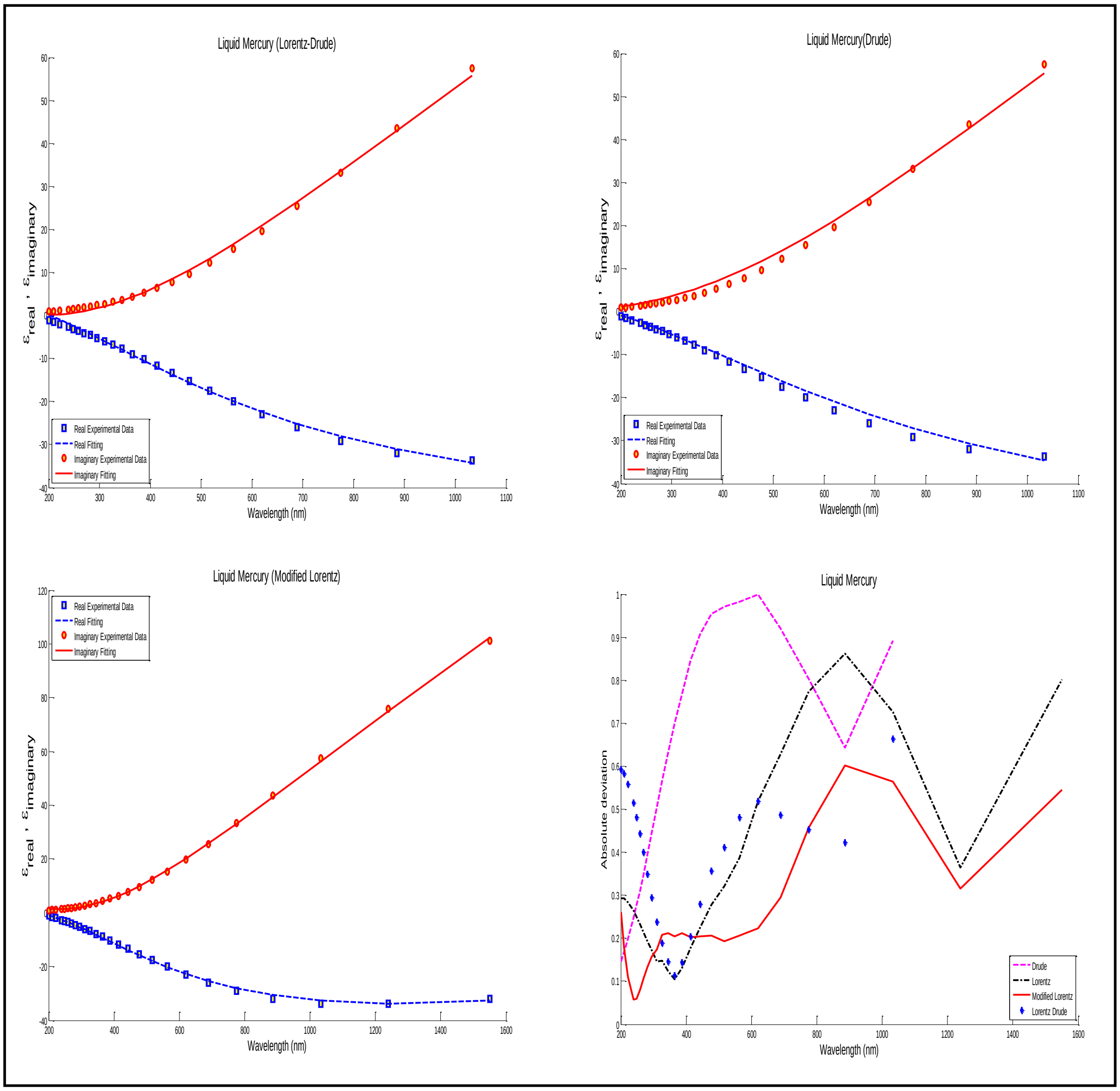

FIG. 5-5 Comparison between modeled and experimental complex permittivities of liquid mercury

The number of pole pairs used for different models are: 2 for Lorentz model, 2 for modified Lorentz model, 1for Drude model, 1 Lorentz term and 1 Drude term for Lorentz-Drude model.

The applicability ranges in terms of wavelength are: 200-1550 nm for Lorentz and modified Lorentz models, 200-1040 nm for Drude and Lorentz-Drude models.

From the normalized absolute deviation curves it is observed that the modified Lorentz model has the best accuracy among the models used for liquid mercury. So, use of the modified Lorentz model in the FDTD algorithm will give more accurate outputs while the use of Drude model will make the algorithm faster.

Indium phosphide:

Lorentz, modified Lorentz and Lorentz-Drude models have been used to model the frequency dependent permittivity of indium phosphide. FIG. 5-6 shows that for all the models, the optimized permittivity curves have very good agreement with the experimental curves.

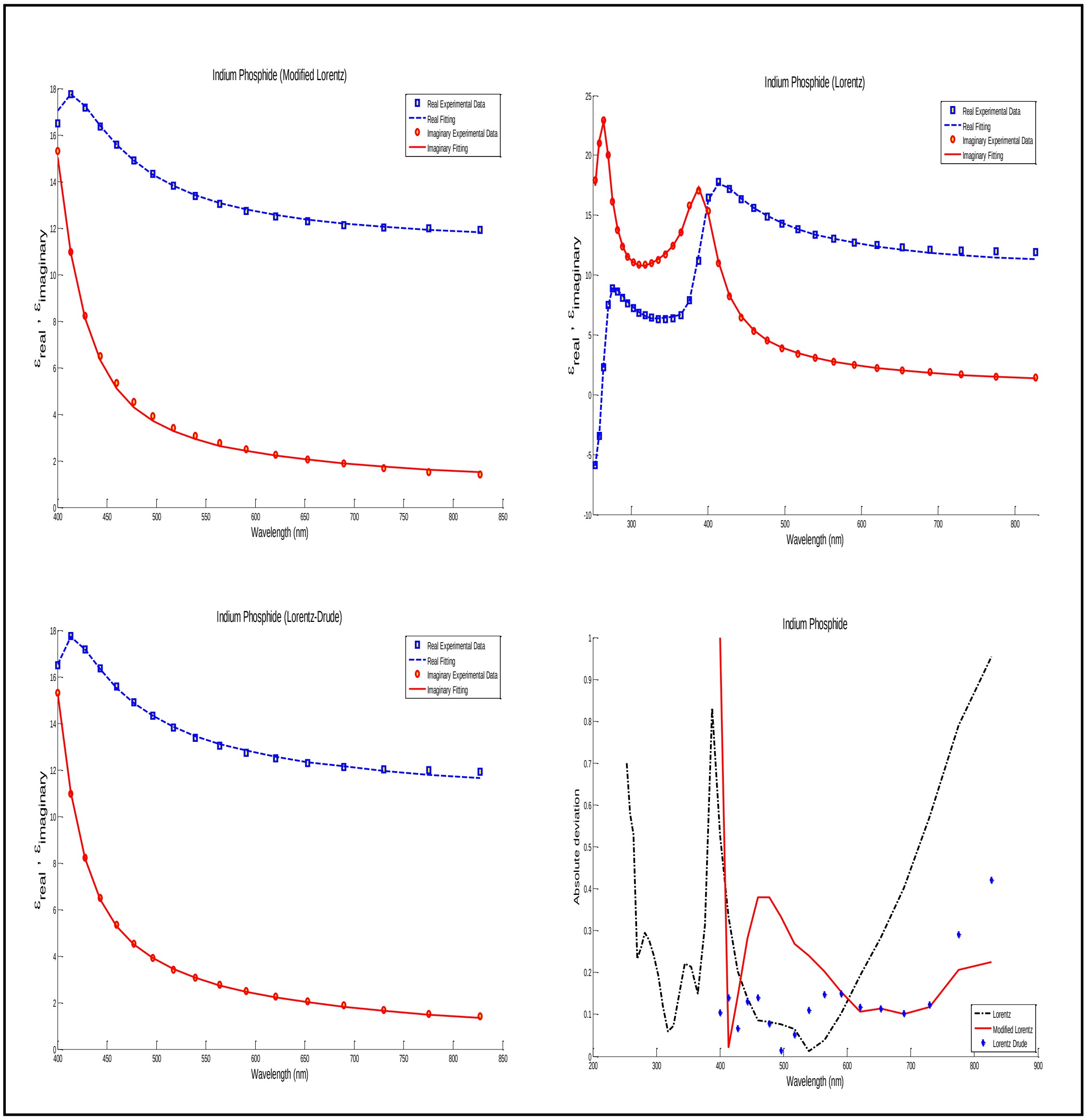

FIG. 5-6 Comparison between modeled and experimental complex permittivities of indium phosphide

The number of pole pairs used for Lorentz and modified Lorentz models are 4 and 2 respectively. For the Lorentz-Drude model, we used 1 Drude term and 2 Lorentz terms.

The fitting is applicable over wavelength ranges of 250-830 nm for Lorentz model and 400-830 nm for modified Lorentz and Lorentz-Drude models.

From the normalized absolute deviation curves it can be observed that different models show better accuracy in different wavelength ranges. For example, the Lorentz model gives the least accuracy beyond 600 nm but has better accuracy compared to other models in the 430-600 nm range.

Mercury cadmium telluride :

The frequency dependent permittivity of mercury cadmium telluride has been characterized using Lorentz and modified Lorentz models. FIG. 5-7 shows that for both the models, there is very good agreement between the optimized and experimental permittivities.

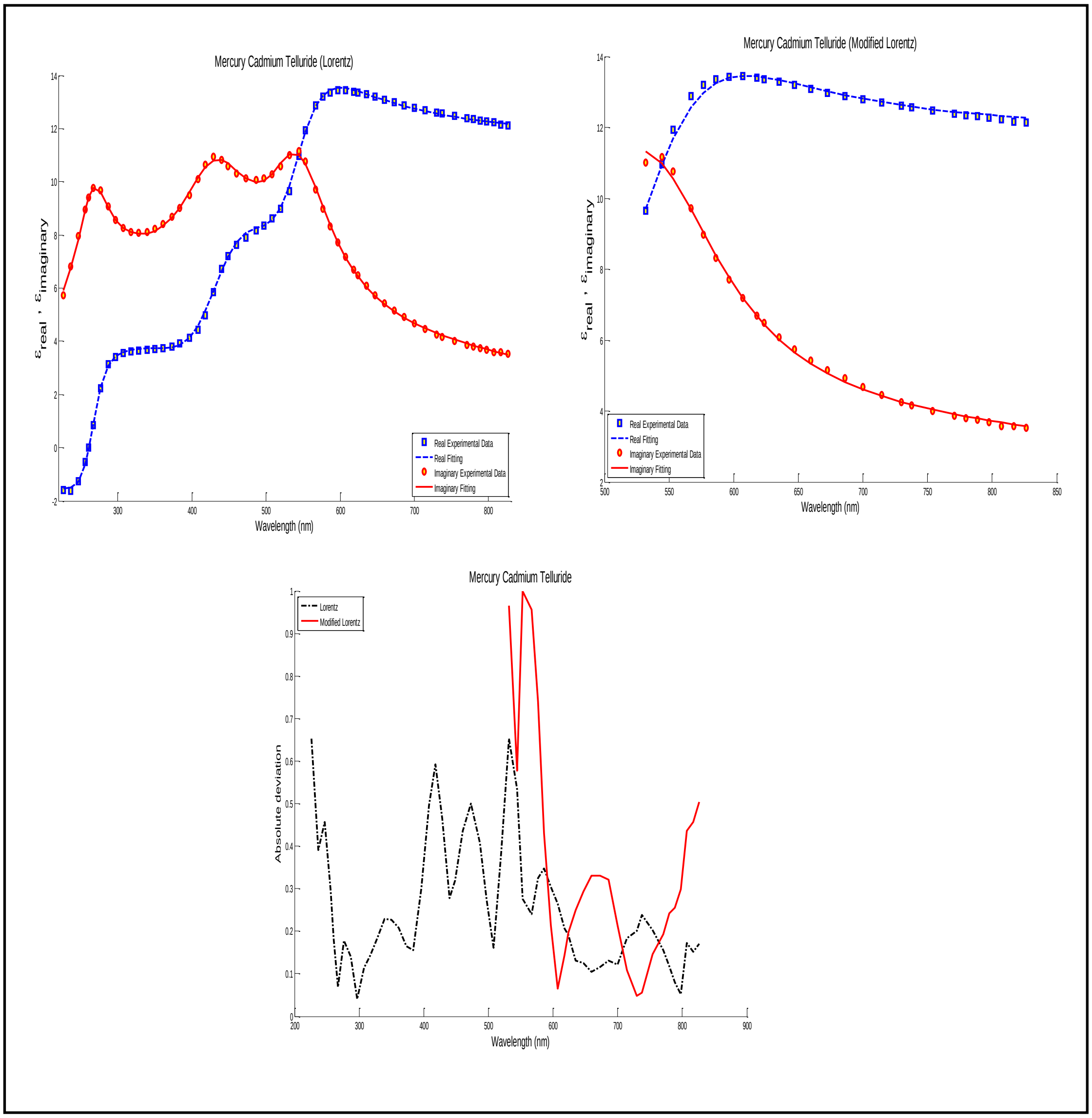

FIG. 5-7 Comparison between modeled and experimental complex permittivities of mercury cadium telluride

4 pole pairs are used for Lorentz model and 2 for modified Lorentz model.

The applicability ranges in terms of wavelength are: 220-830 nm for Lorentz model and 530-830 nm for modified Lorentz model.

Both the accuracy and applicability range for modified Lorentz model is less compared to those for the Lorentz model.

Molybdenum:

The frequency dependent permittivity of molybdenum has been characterized using Lorentz, modified Lorentz, Drude and Lorentz-Drude models. FIG. 5-8 shows that for all the models, the optimized permittivity curves have very good agreement with the experimental curves.

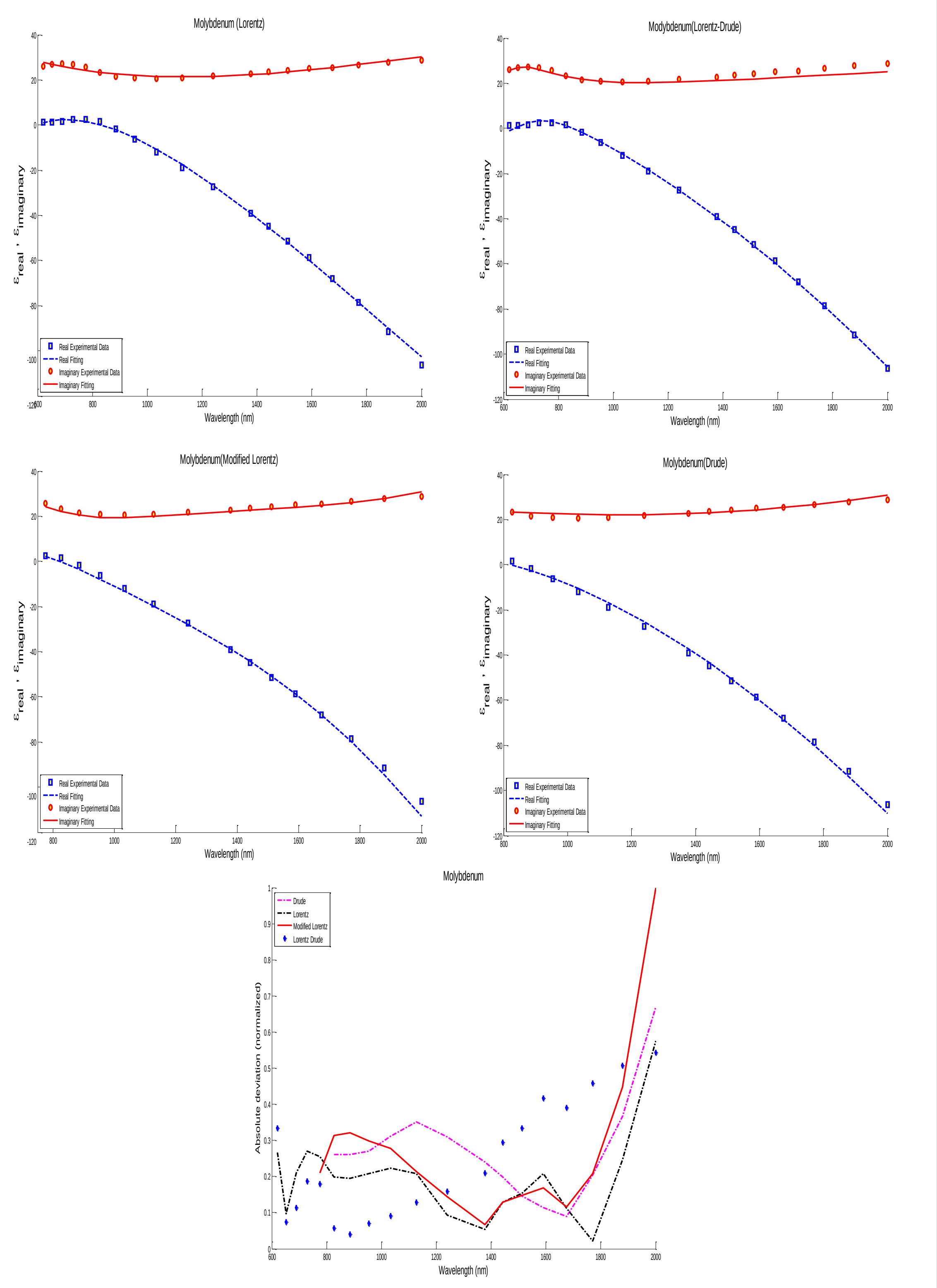

FIG.5-8 Comparison between modeled and experimental complex permittivities of molybdenum

The number of pole pairs used for Lorentz, modified Lorentz and Drude model are 4, 4 and 3 respectively. For the Lorentz-Drude model, we used 1 Drude term and 2 Lorentz terms.

The fitting is applicable over wavelength ranges of 615-2000 nm for Lorentz and Lorentz-Drude models, 770-2000 nm for modified Lorentz model and 820-2000 nm for Drude model.

From the normalized absolute deviation curves we see that the Lorentz-Drude model is the most accurate in the wavelength range of 650-1200 nm while the Lorentz model has the best accuracy in the range of 1200-2000 nm.

So, selection of a model for better accuracy depends on the wavelength range of interest.

Osmium:

The experimental permittivity curves for osmium have been fitted using Lorentz, Lorentz-Drude and Drude models over wavelength ranges of 800-2000 nm, 670-1770 nm and 850-1910 nm respectively. FIG. 5-9 shows that for both the models, there is very good agreement between the optimized and experimental permittivities.

The number of pole pairs used are: 3 for Lorentz model, 3 for Drude model, 1 Drude term and 4 Lorentz terms for Lorentz-Drude model.

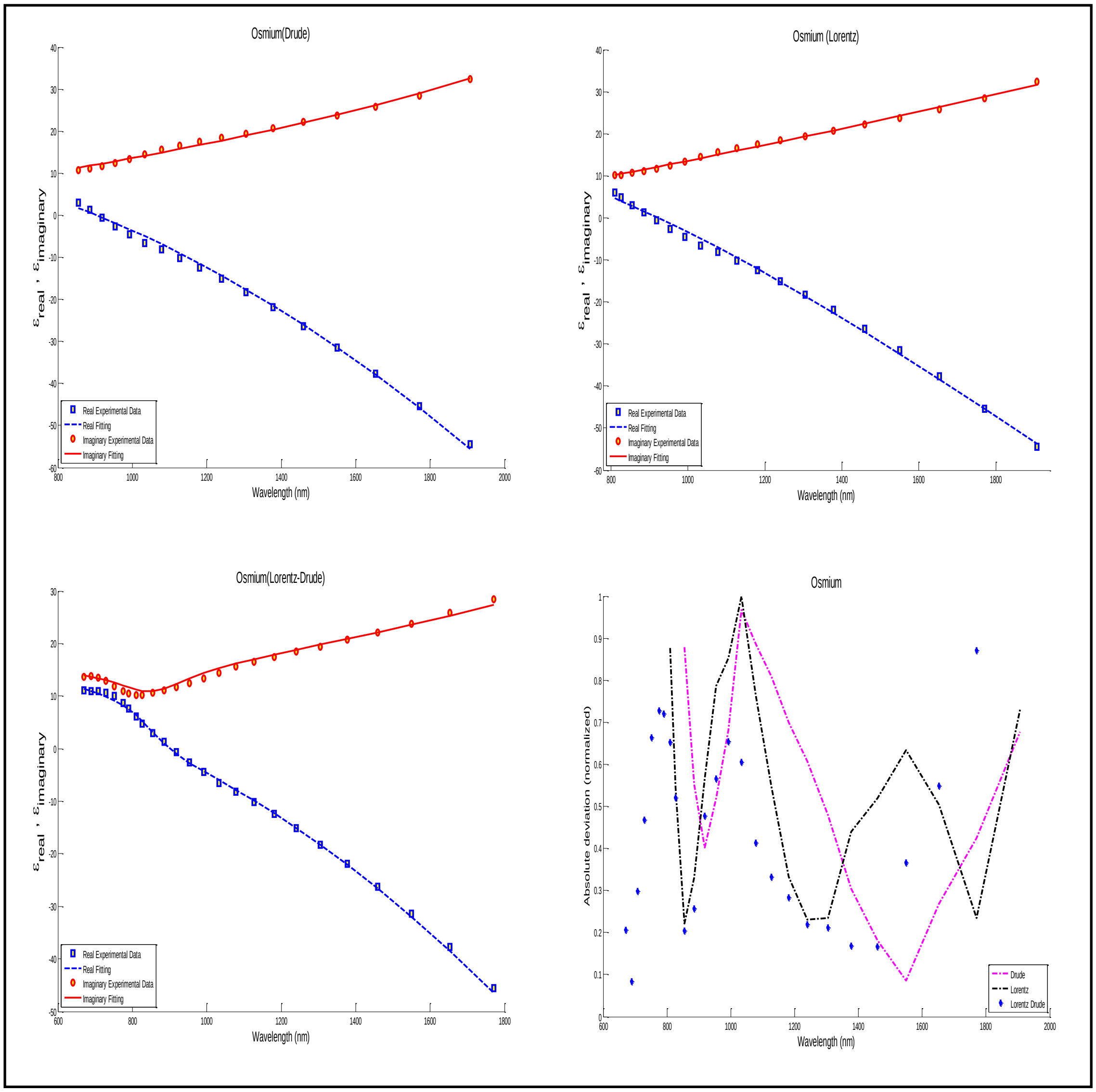

FIG. 5-9 Comparison between modeled and experimental complex permittivities of osmium

The Lorentz -Drude model shows the best accuracy for most part of the wavelength range, especially between 800 nm and 1450 nm. Besides, the Lorentz-Drude modeling for Osmium is valid for a longer wavelength range compared to other models.

Lead sulphide :

The experimental permittivity curves for lead sulphide have been fitted using Lorentz and modified Lorentz models using 5 and 4 pole pairs respectively over an wavelength range of 200-2000 nm. FIG.5-10 shows that for both the models, there is very good agreement between the optimized and experimental permittivities.

From the normalized absolute deviation curves we see that in the wavelength range of 500-1380 nm, the Lorentz model has better accuracy while the modified Lorentz model is more accurate beyond 1400 nm.

So, selection of a model for better accuracy depends on the wavelength range of interest.

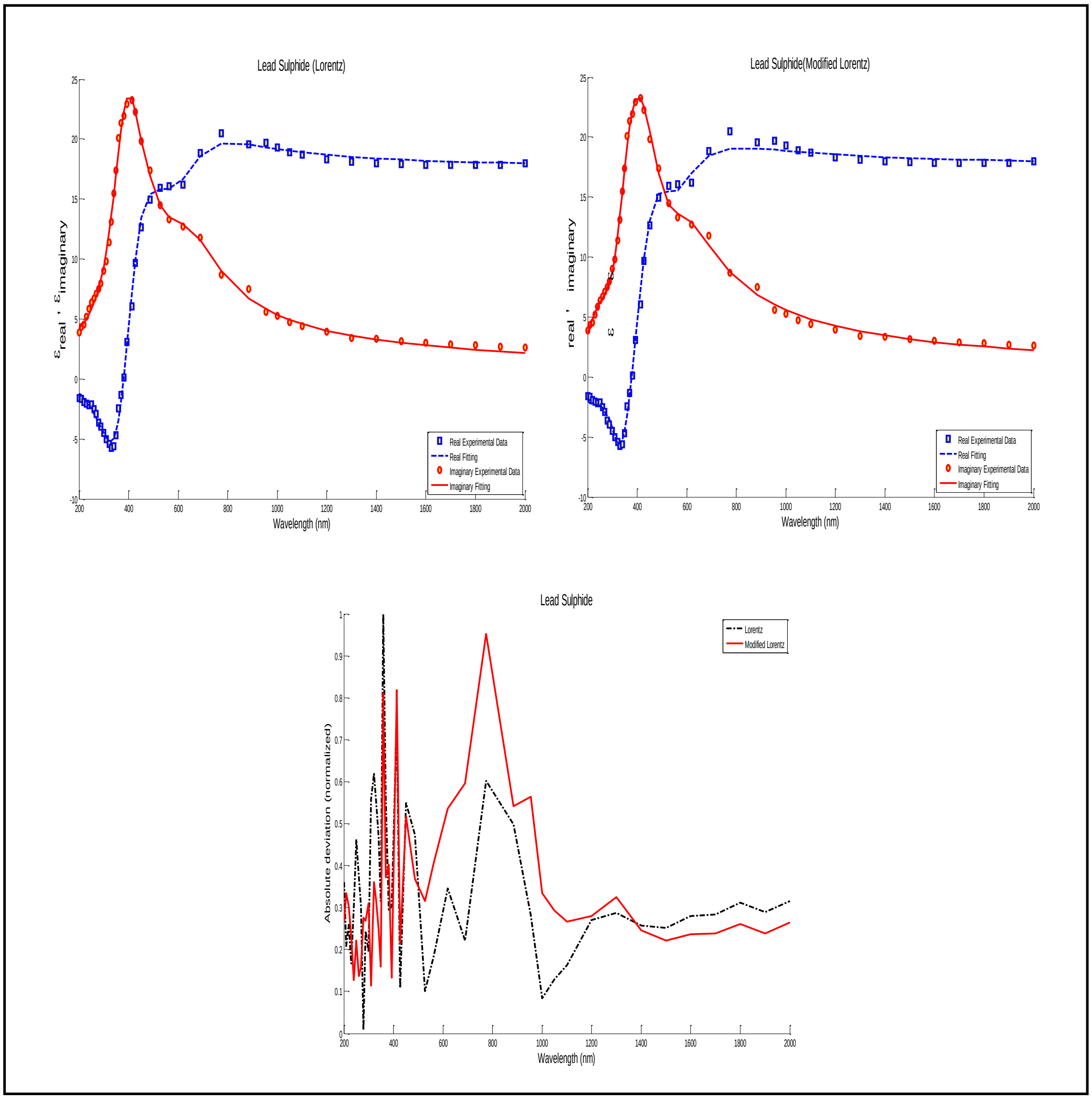

FIG. 5-10. Comparison between modeled and experimental complex permittivities of lead sulphide

Lead selenide:

The modeling for lead selenide has been performed using Lorentz and modified Lorentz models in the wavelength ranges of 300-1080 nm and 300-780 nm. FIG. 5-11 shows that for both the models, the optimized permittivity curves have very good agreement with the experimental curves.

The number of pole pairs used for Lorentz and modified Lorentz models are 6 and 4 respectively.

The normalized absolute deviation is less in case of Lorentz model and the range of wavelength over which it is applicable is also longer compared to that for the modified Lorentz model.

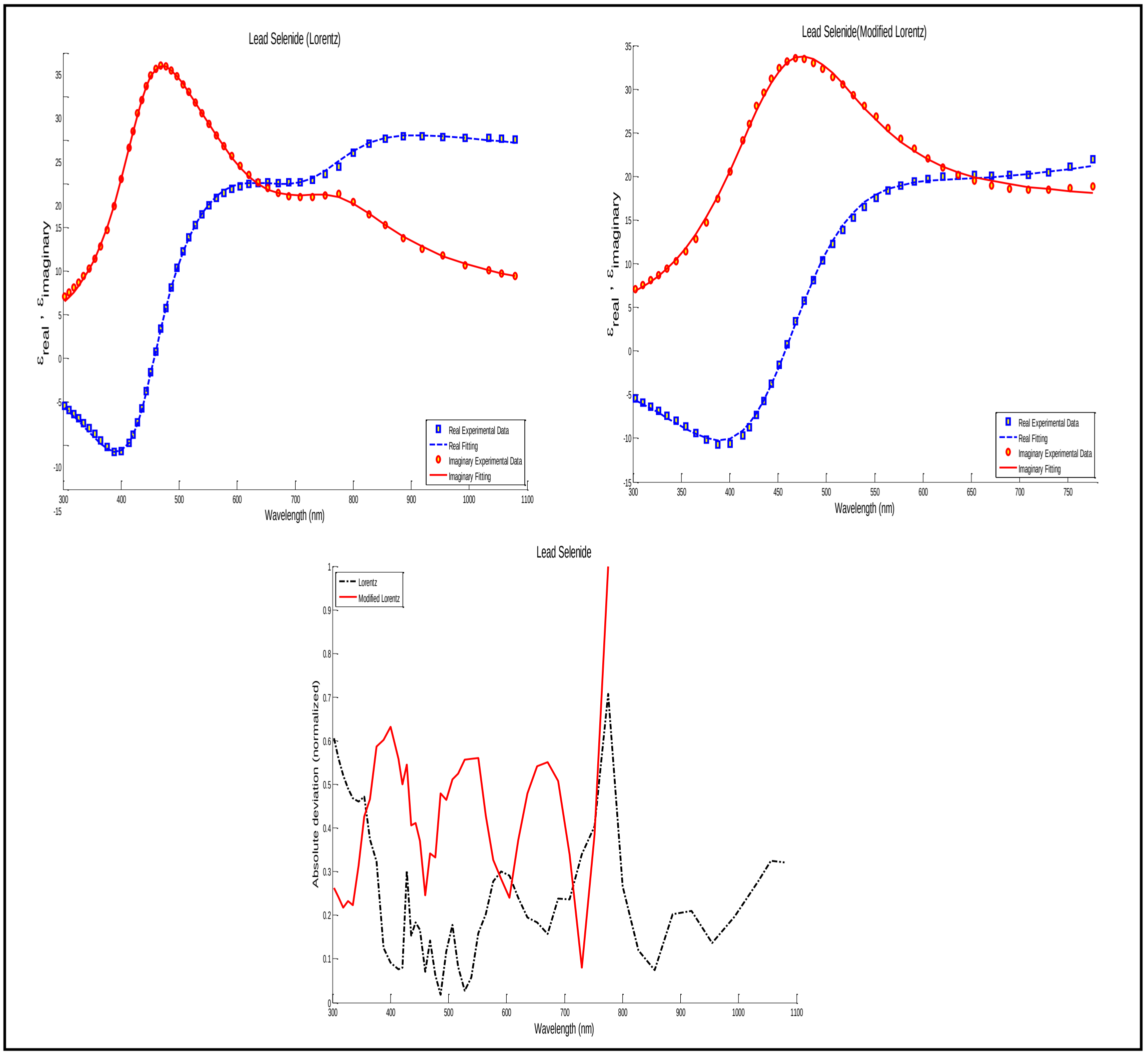

FIG. 5-11 Comparison between modeled and experimental complex permittivities of lead selenide

Rhodium:

The experimental permittivity curves for rhodium have been fitted using Lorentz and Drude models using 3 and 2 pole pairs respectively over an wavelength range of 400-1770 nm. FIG.5-12 shows that for both the models, the optimized permittivity curves have very good agreement with the experimental curves.

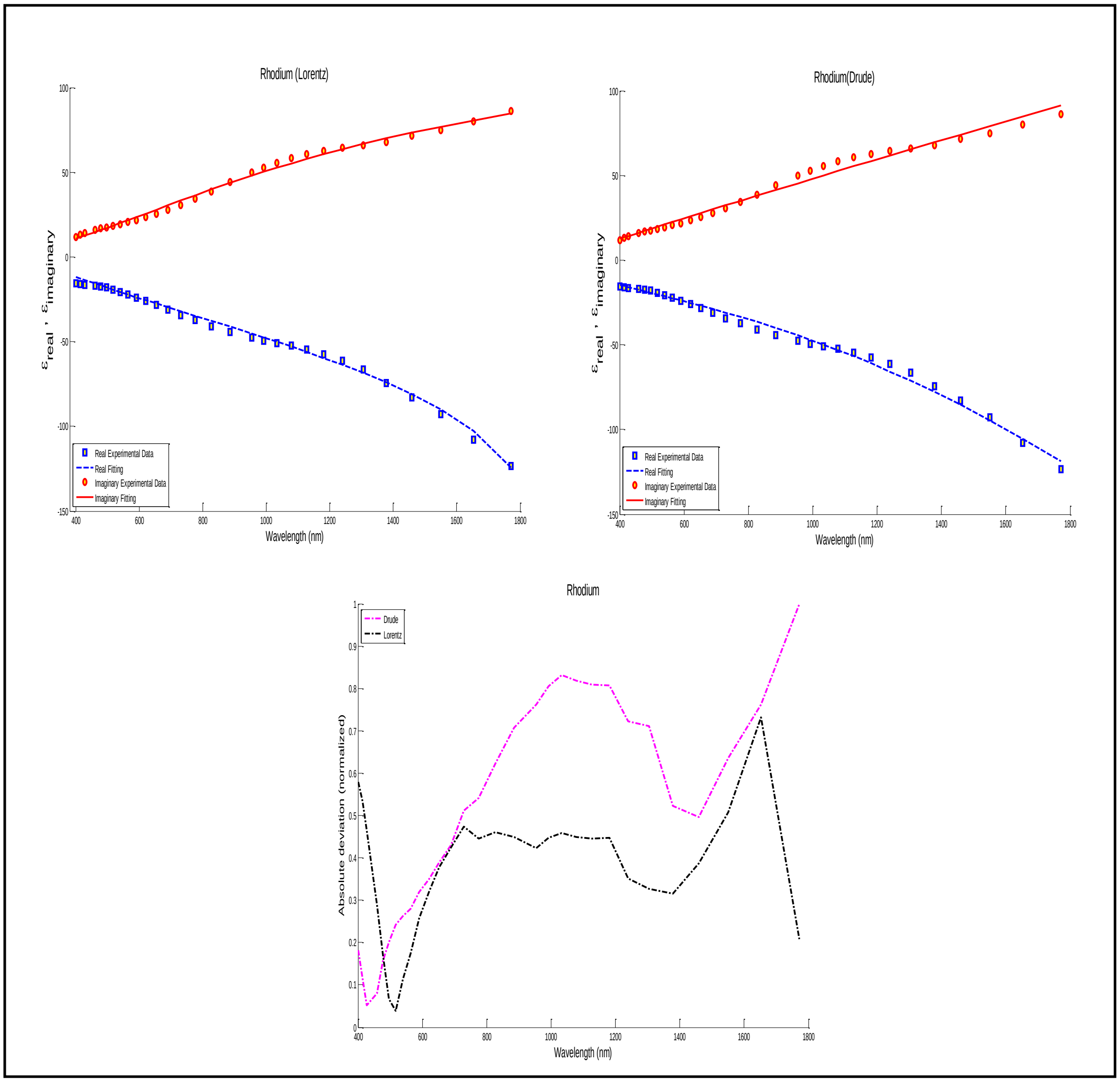

FIG. 5-12 Comparison between modeled and experimental complex permittivities of rhodium

For rhodium, the Lorentz model has better accuracy compared to the Drude model.

Tantalum:

Lorentz, modified Lorentz, Drude and Lorentz-Drude models have been used to model the frequency dependent permittivity of tantalum. FIG. 5-13 shows that for all the models, the optimized permittivity curves have very good agreement with the experimental curves.

The number of pole pairs used for Lorentz, modified Lorentz and Drude model are 2, 4 and 3 respectively. For the Lorentz-Drude model, we used 1 Drude term and 1 Lorentz term.

The fitting is applicable over wavelength ranges of 620-1600 nm for modified Lorentz and Lorentz-Drude models, 600-2000 nm for Lorentz model and 620-2000 nm for Drude model.

The Lorentz model has better accuracy compared to the other models for most part of the wavelength range. Besides, it uses the least number of pole pairs and also is valid over a longer wavelength range compared to the other models.

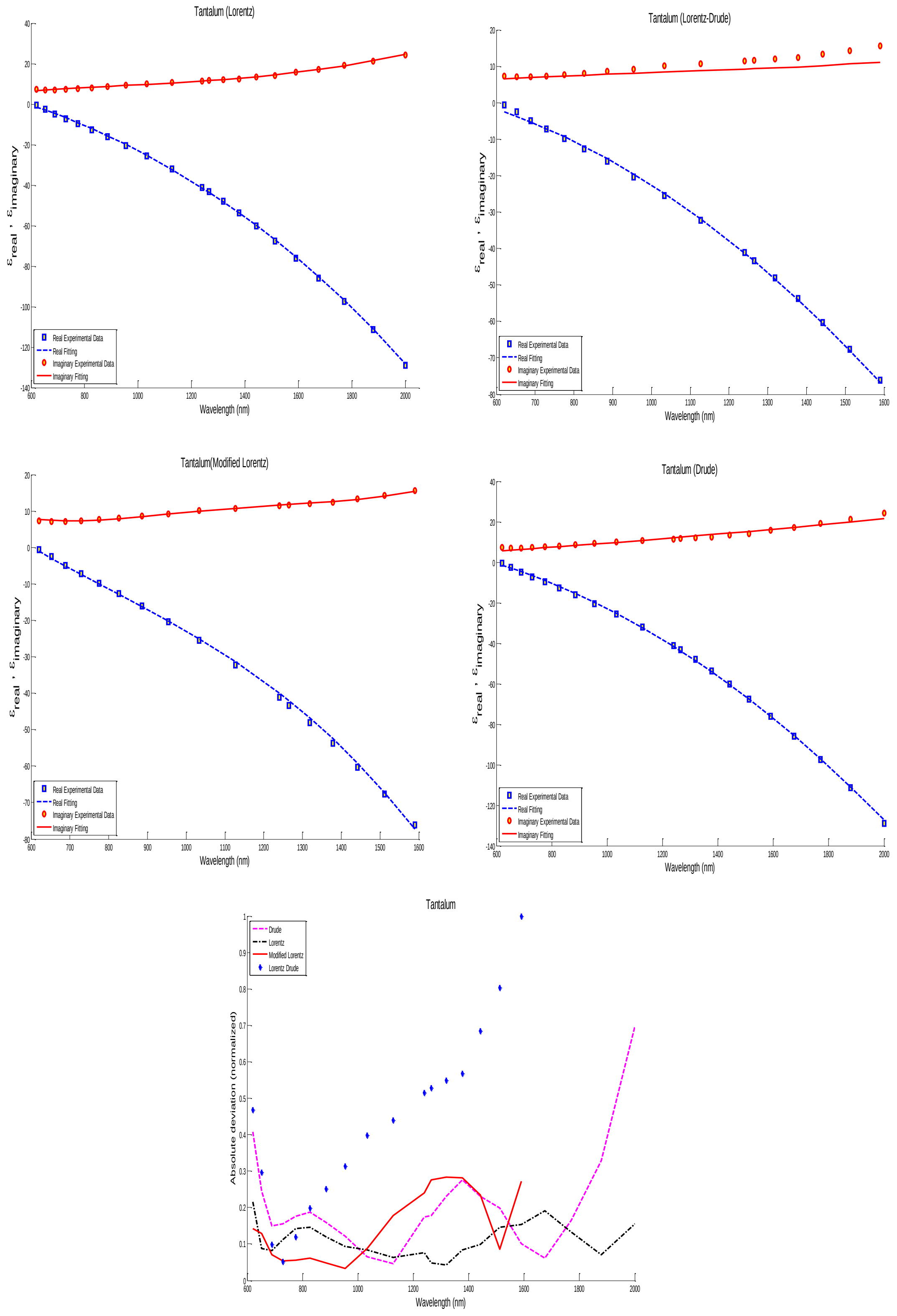

FIG. 5-13 Comparison between modeled and experimental complex permittivities of tantalum

Thulium:

The experimental permittivity curves for thulium have been fitted using Lorentz, modified Lorentz and Drude models using 3,4 and 4 pole pairs respectively. FIG.5-14 shows that for both the models, there is very good agreement between the optimized and experimental permittivities.

The applicability ranges in terms of wavelength are 400-1050 nm for Lorentz model and 500-1050 nm for modified Lorentz and Drude models.

For most part of the wavelength range, the modified Lorentz model has the best accuracy among the models used for thulium.

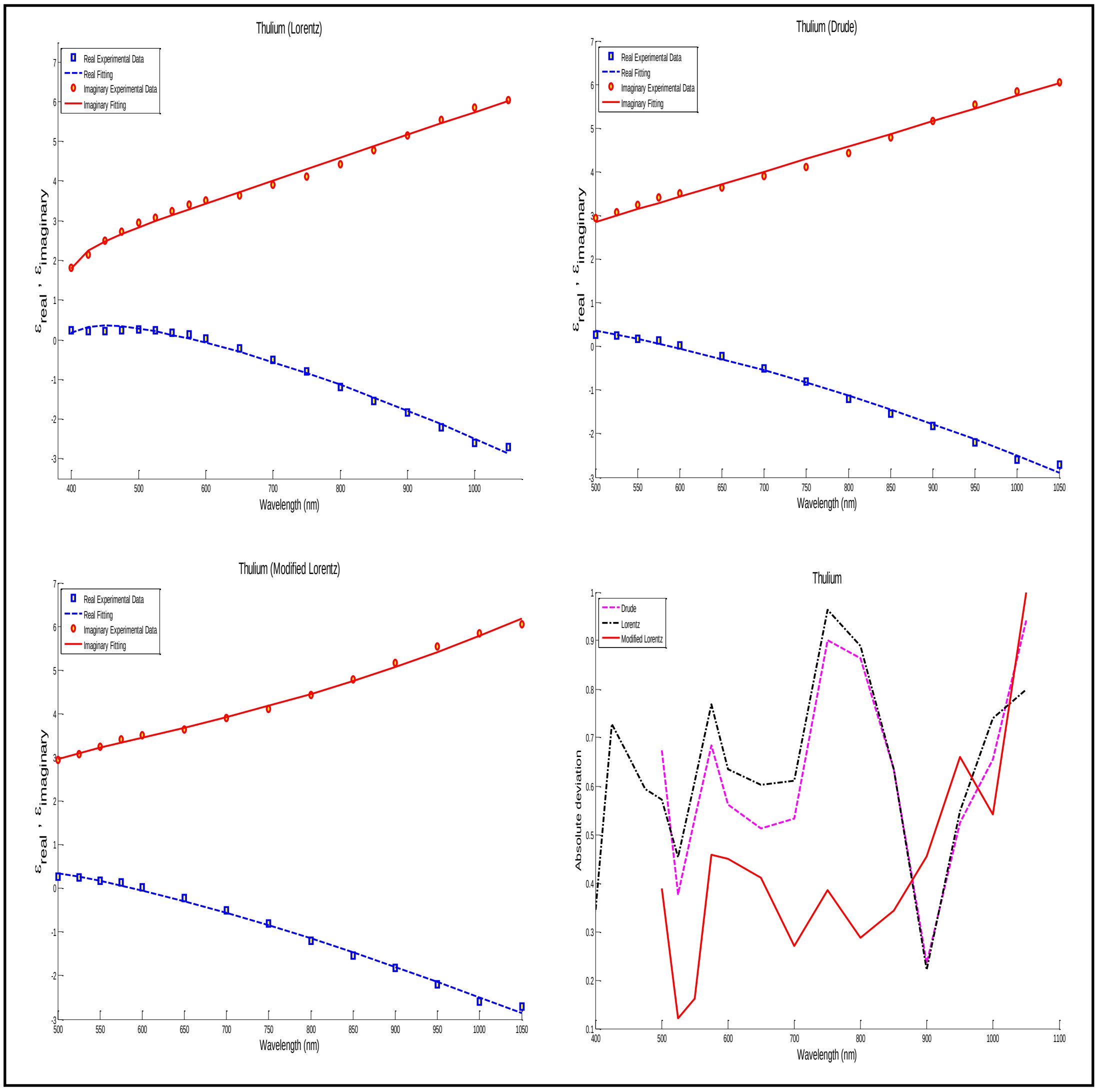

FIG. 5-14 Comparison between modeled and experimental complex permittivities of Thulium

Zirconium nitride:

Lorentz and modified Lorentz models have been used to characterize the frequency dependent permittivity of zirconium nitride. FIG.5-15 shows that for both the models, the optimized permittivity curves have very good agreement with the experimental curves.

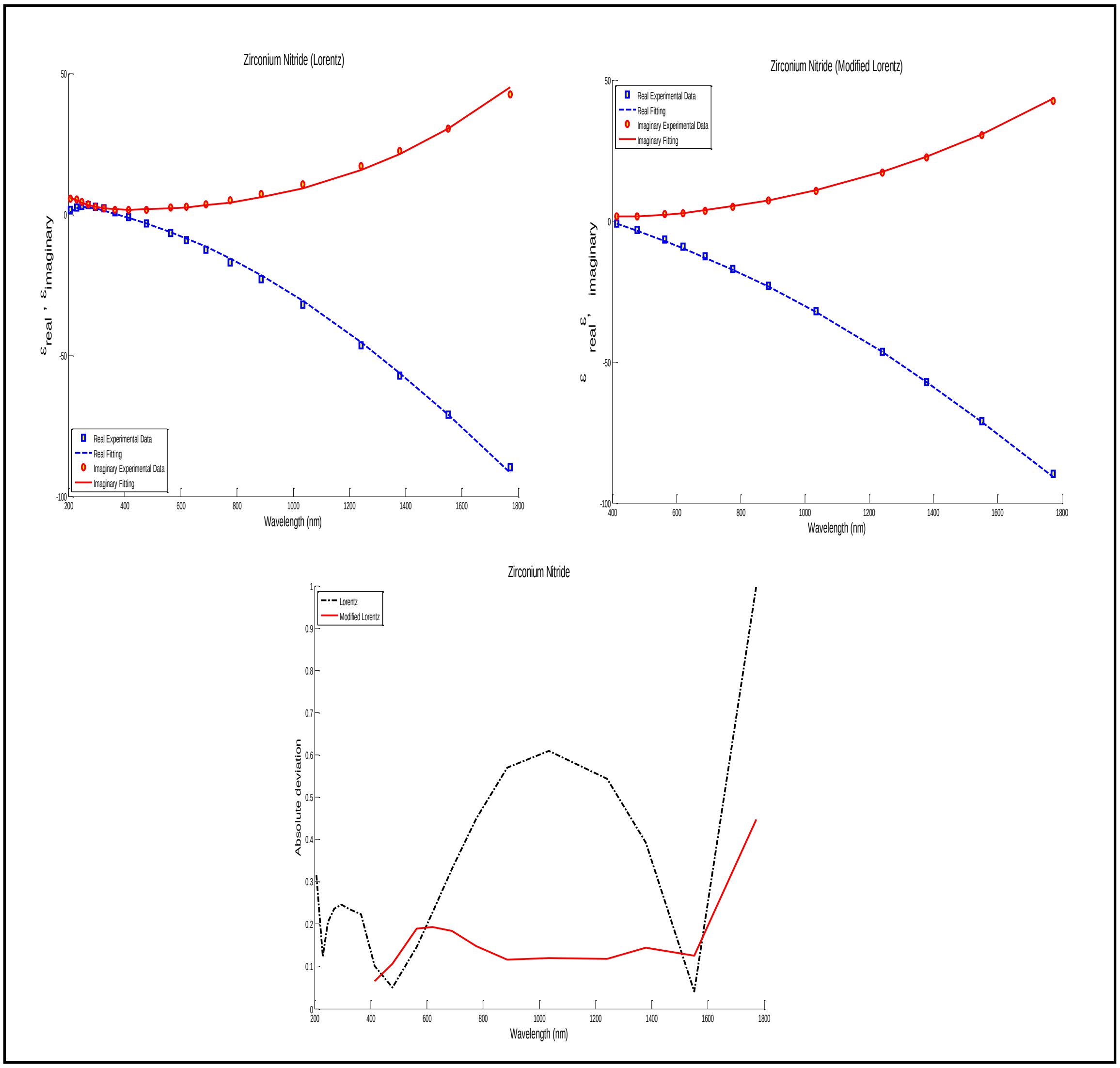

FIG. 5-15 Comparison between modeled and experimental complex permittivities of zirconium nitride

The number of pole pairs used for Lorentz model is 2 and that for modified Lorentz model is 3. The fitting is applicable over wavelength range of 200-1800 nm for Lorentz model and 410-1780 nm for modified Lorentz model.

For most part of the wavelength range, the modified Lorentz model has the better ccuracy compared to the Lorentz model.

Titanium nitride:

The experimental permittivity curves for titanium nitride have been fitted using Lorentz and modified Lorentz models using 3 and 4 pole pairs respectively. FIG.5-16 shows that for both the models, the optimized permittivity curves have very good agreement with the experimental curves.

The applicability ranges in terms of wavelength are 350-1900 nm for Lorentz model and 400-1130 nm for modified Lorentz model.

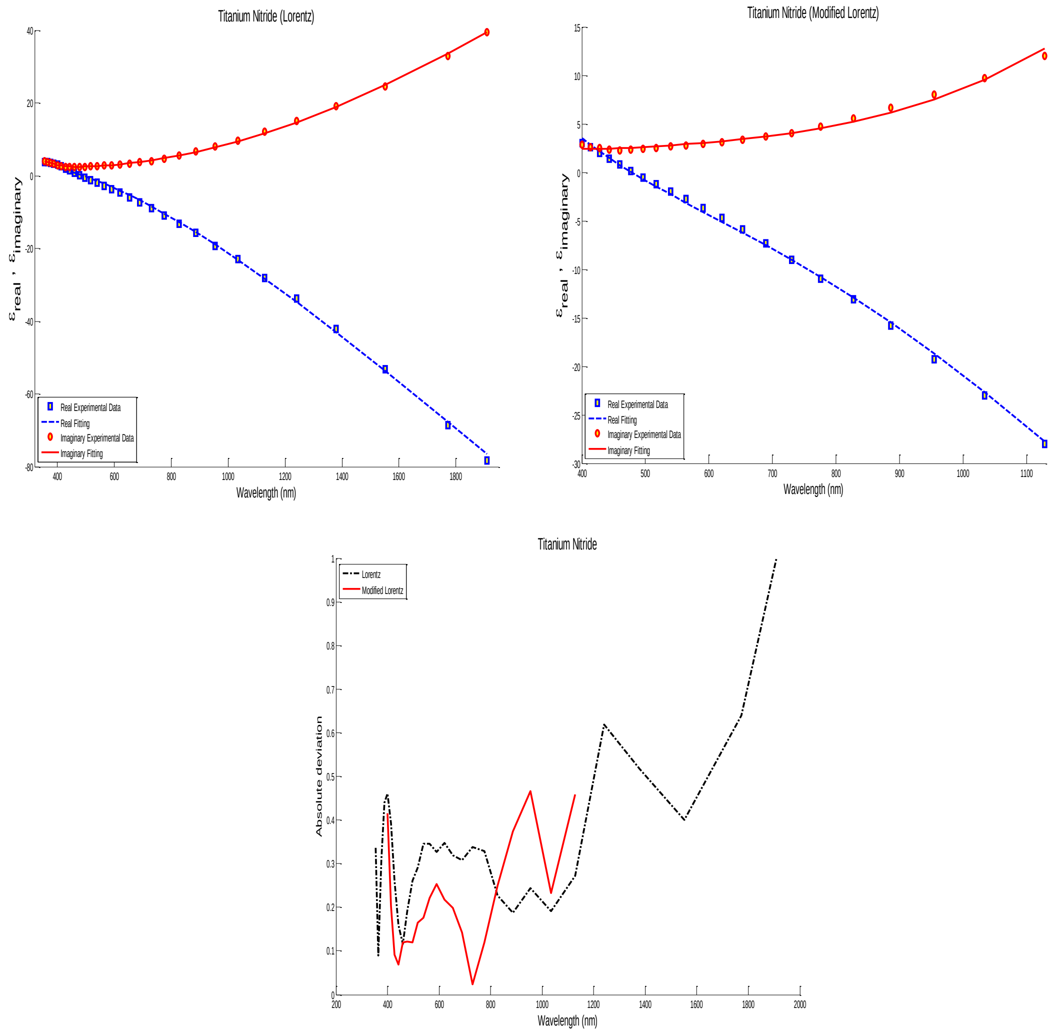

FIG. 5-16 Comparison between modeled and experimental complex permittivities of titanium nitride

In the wavelength range of 400-800 nm, the modified Lorentz model has better accuracy. So, if the wavelength range of interest is limited to 400-800 nm, modified Lorentz model should be used.

Beyond this range, the Lorentz model has to be used.

Chapter 6

Propagation of SPP in Nanostructure

6.1 Developing the Simulation Model

We have developed a simulation model based on the FDTD algorithm proposed by Yee [40]. But the original formulation of Yee assumes that the permittivity, permeability etc. of materials are independent of frequency which is not true in real cases. So, in order to incorporate the frequency dependency of material properties we have used the FDTD algorithm based on the general Auxiliary Differential Equation (ADE) method [41]. In order to prevent reflections of the propagating wave from the boundary of the simulation region, we have used the Perfectly Matched Layer (PML) [42].

The frequency dependent electric flux density is given by

$$D(\omega) = \varepsilon_0 \varepsilon_\infty E(\omega) + P(\omega) \tag{6.1}$$

Again the general form of the Lorentz model is

$$P(\omega) = \frac{a}{b + jc\omega - d\omega^2} E(\omega) \tag{6.2}$$

Using inverse Fourier transform equation (6.2) can be written as

$$bP(t) + cP'(t) + dP''(t) = aE(t) \tag{6.3}$$

For first order polarization the FDTD solution of equation (6.3) can be expressed as

$$P^{n+1} = C_1 P^n + C_2 P^{n-1} + C_3 E^n \tag{6.4}$$

where

$$C_1 = \frac{4d - 2b\Delta t^2}{2d + c\Delta t} \tag{6.5}$$

$$C_2 = \frac{-2d - c\Delta t}{2d + c\Delta t} \tag{6.6}$$

$$C_3 = \frac{2a\Delta t^2}{2d+c\Delta t} \tag{6.7}$$

The values of C_1, C_2, C_3 will be different for different materials.

The values of electric flux density and polarization obtained from (6.1) and (6.4) can be used to find out the electric field intensity as follows

$$E^{n+1} = \frac{D^{n+1} - \sum_{i=1}^{N} P_i^{n+1}}{\varepsilon_0 \varepsilon_\infty} \tag{6.8}$$

where N is the number of pole pairs and D^{n+1} is the updated value of the electric flux density.

6.2 Validating the Developed Simulation Model

We have simulated the broadening of signal passing through a one-dimensional dispersive material using the parameters mentioned in [26]. The parameters used are $\varepsilon_\infty = 2.25$, ε_0=5.25, ω_0= $4\times10^{14}(rad/s)$, δ=2×10^9(rad/s),

The result obtained using the developed simulation model is compared with the result provided in [26]. An excellent agreement is found between the two results as shown in the following figure:

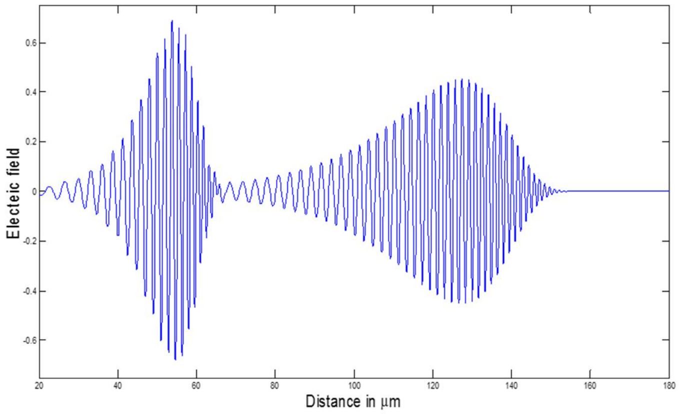

(a)

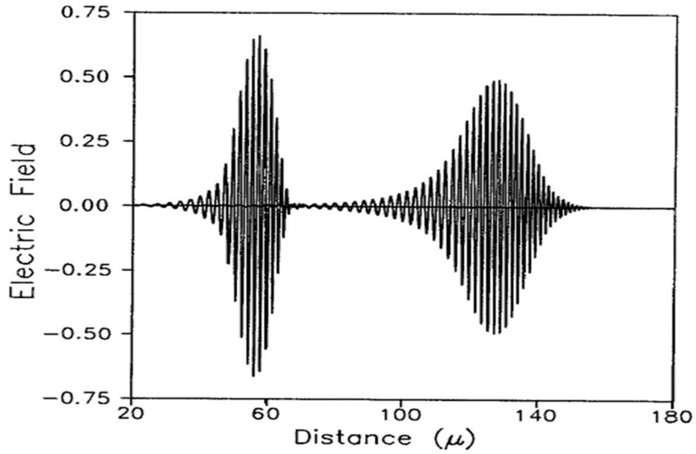

(b)

Fig. 6-1: Comparison between the results obtained from simulation (a) and the result given in [26] (b)

6.3 SPP Propagation in Single Metal-Dielectric Interface

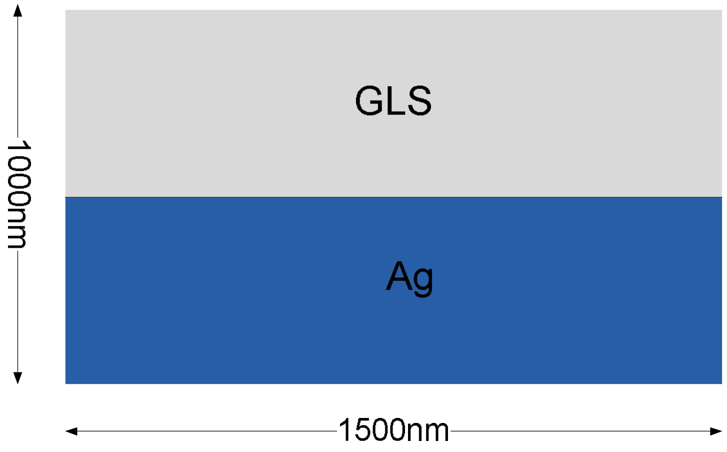

Figure 6-2: Gallium Lanthanum Sulphide (GLS) and Silver interface

A single metal-dielectric interface is simulated for SPP propagation. The metal layer is formed using Silver and the dielectric layer is formed using Gallium Lanthanum Sulphide. The modeling parameters of silver are taken from [12] and that of GLS are taken from [43].

Theoretically the rate of decay in metal is higher than the decay rate in dielectric. The simulated outputs shown in figure 6-3 also verify this fact.

During simulation the size of each cell was taken as 5nm in both horizontal and vertical directions. So, in figure 6-3, the interface between the GLS and Silver layers is along the 100th cell. The cells (in the vertical direction) from the beginning upto the 100th form the Silver layer and cells from the 100th to the end form the GLS layer. From the simulated E_x, E_y and H_z profiles we see that in all cases the profile decays more rapidly in the silver layer compared to the GLS layer.

Again since the decay occurs more rapidly in metal compared to dielectric, it is expected that the field penetration depths in the GLS layer will be more. This is evident from the figures 6-4, 6-5, 6-6. In these figures we see that the E_x, E_y and H_z fields have penetrated further into the GLS layer compared to the Silver layer.

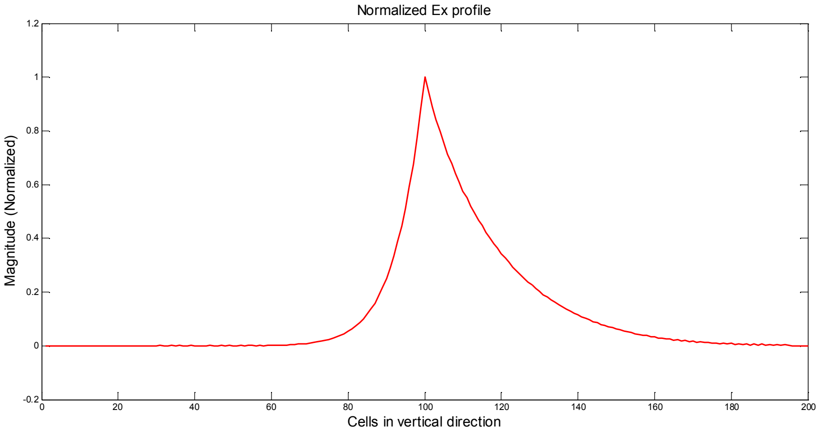

(a)

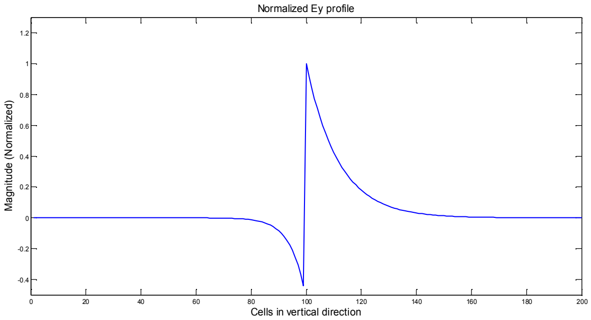

(b)

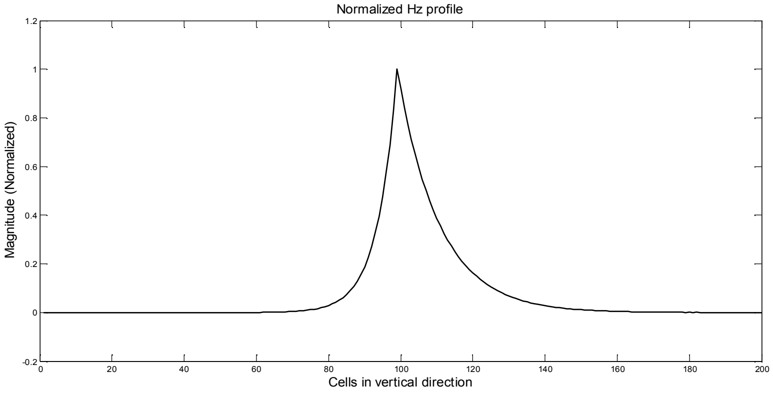

(c)

Figure 6-3: Normalized Ex (a), Ey (b) and Hz (c) profiles for GLS and Silver interface

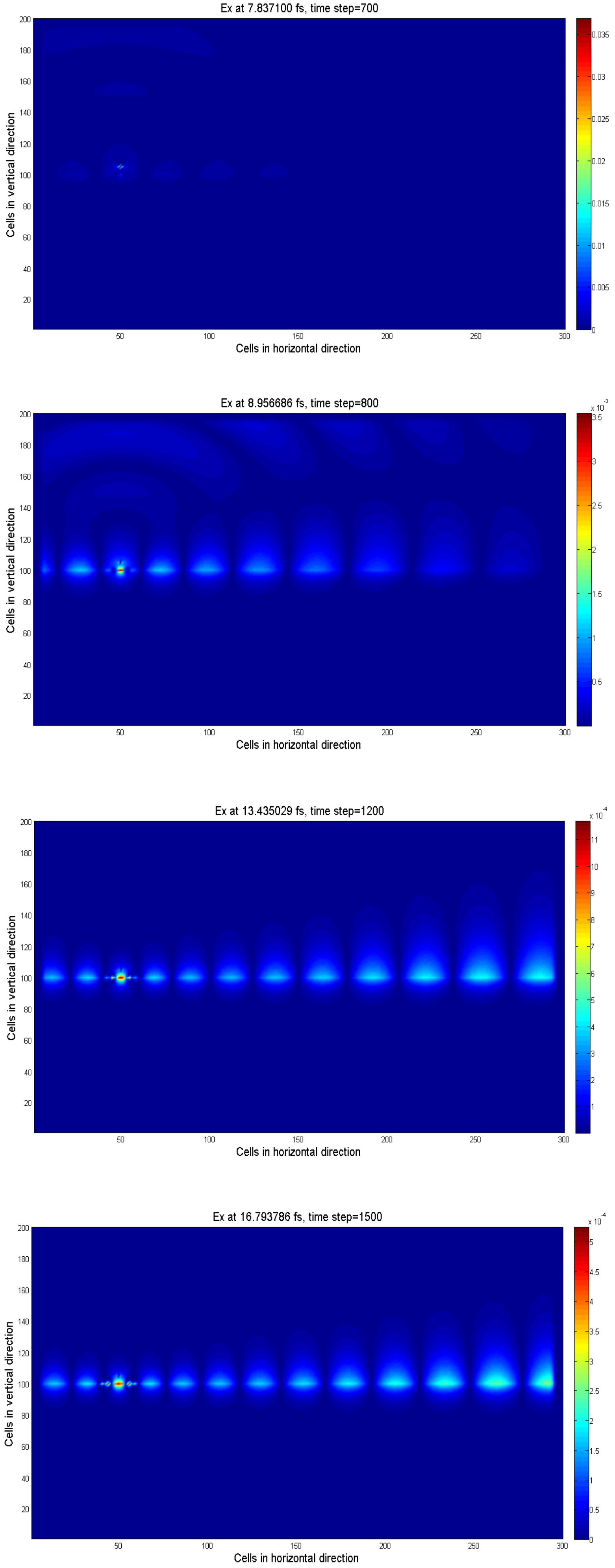

Figure 6-4: 4 snapshots of Ex field distribution at the GLS-Ag interface

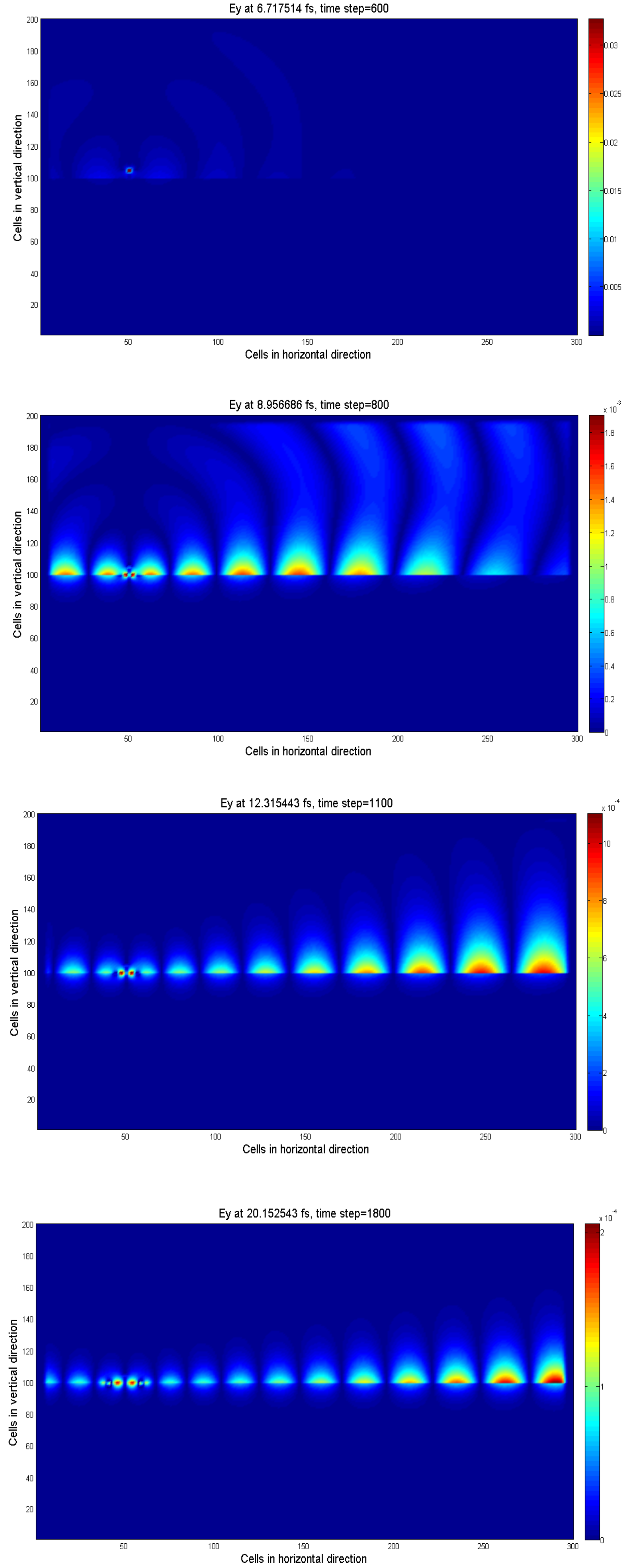
Ey at 6.717514 fs, time step=600

Ey at 8.956686 fs, time step=800

Ey at 12.315443 fs, time step=1100

Ey at 20.152543 fs, time step=1800

Figure 6-5: 4 snapshots of Ey field distribution at the GLS-Ag interface

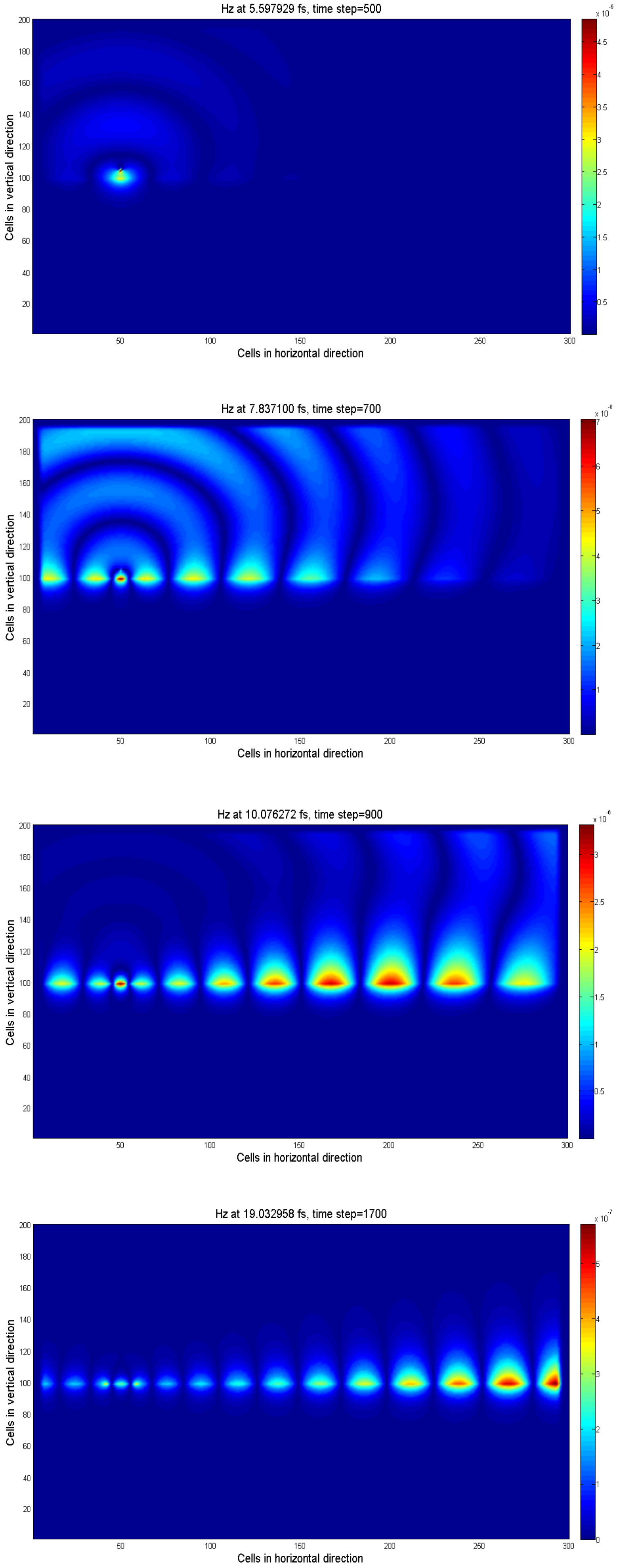

Figure 6-6: 4 snapshots of Hz field distribution at the GLS-Ag interface

6.4 SPP Propagation in Metal-Air-Metal Structure

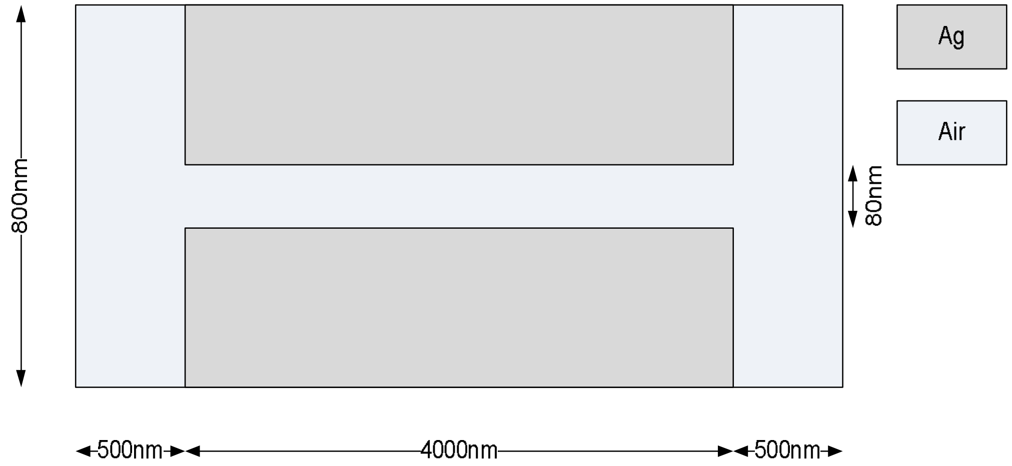

Figure 6-7: Silver-Air-Silver structure for SPP propagation.

A waveguide containing silver and air as shown in figure 6-7 is simulated. During simulation the size of each cell was taken as 5nm in both horizontal and vertical directions. So, the two silver-air interfaces are formed along cell numbers 72 and 88 in the vertical direction. In the vertical direction, the cells from the beginning upto the 72th form the lower Silver layer, the cells from the 72th to the 88th form the air layer, the upper Silver layer is formed by the 88th to the 160th cells.

From the simulated profiles of E_x, E_y, H_z shown in figure 6-8 we can see that the decay is much faster from the two interfaces into the two silver layers compared to that in the air layer.

Since the propagation loss in silver is much higher compared to that in air, so the field distributions remain mainly confined in the air layer as shown in figures 6-9, 6-10, 6-11.

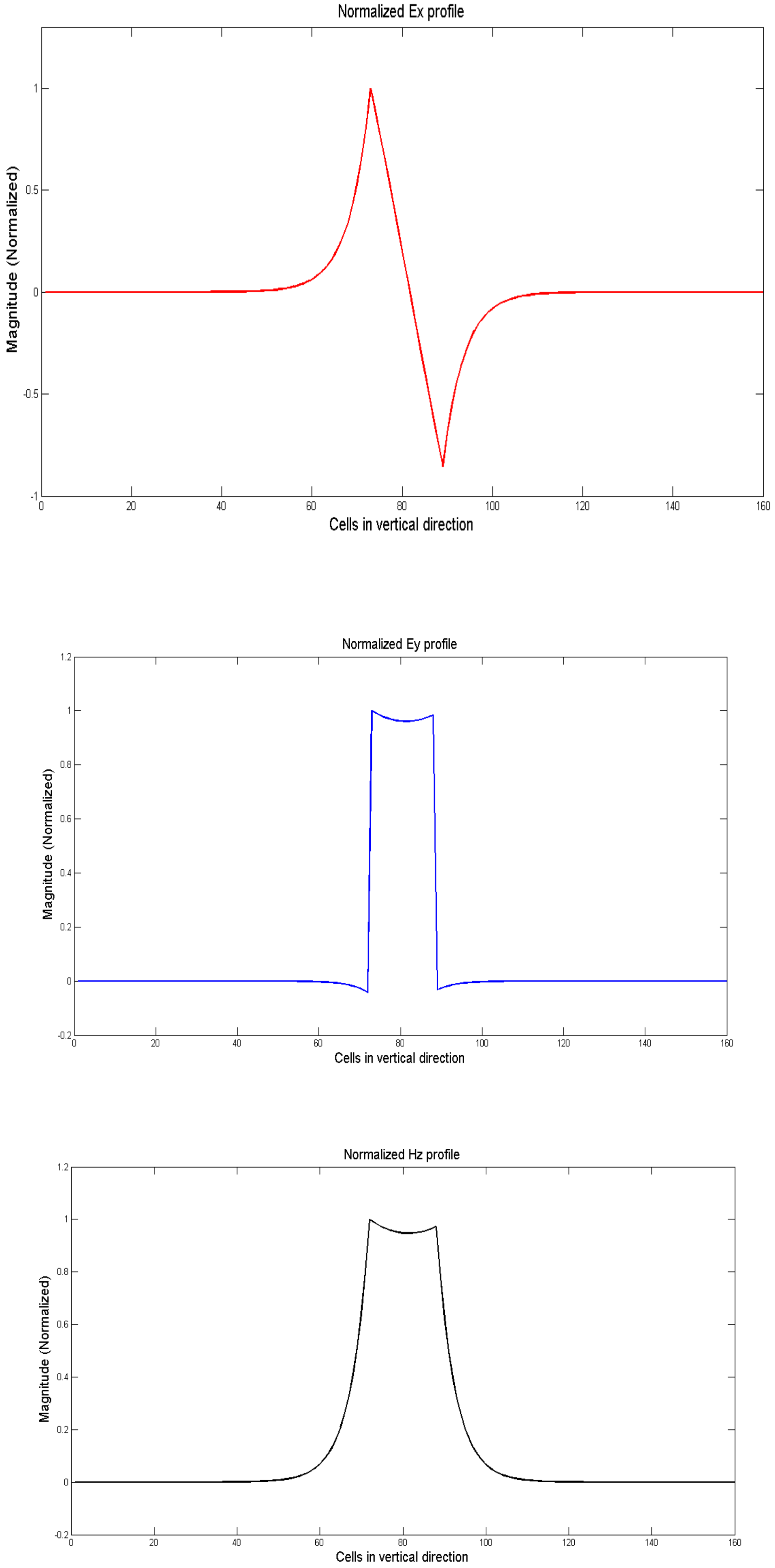

Fig. 6-8 Normalized Ex (a), Ey (b) and Hz (c) profiles for Ag-air-Ag interface

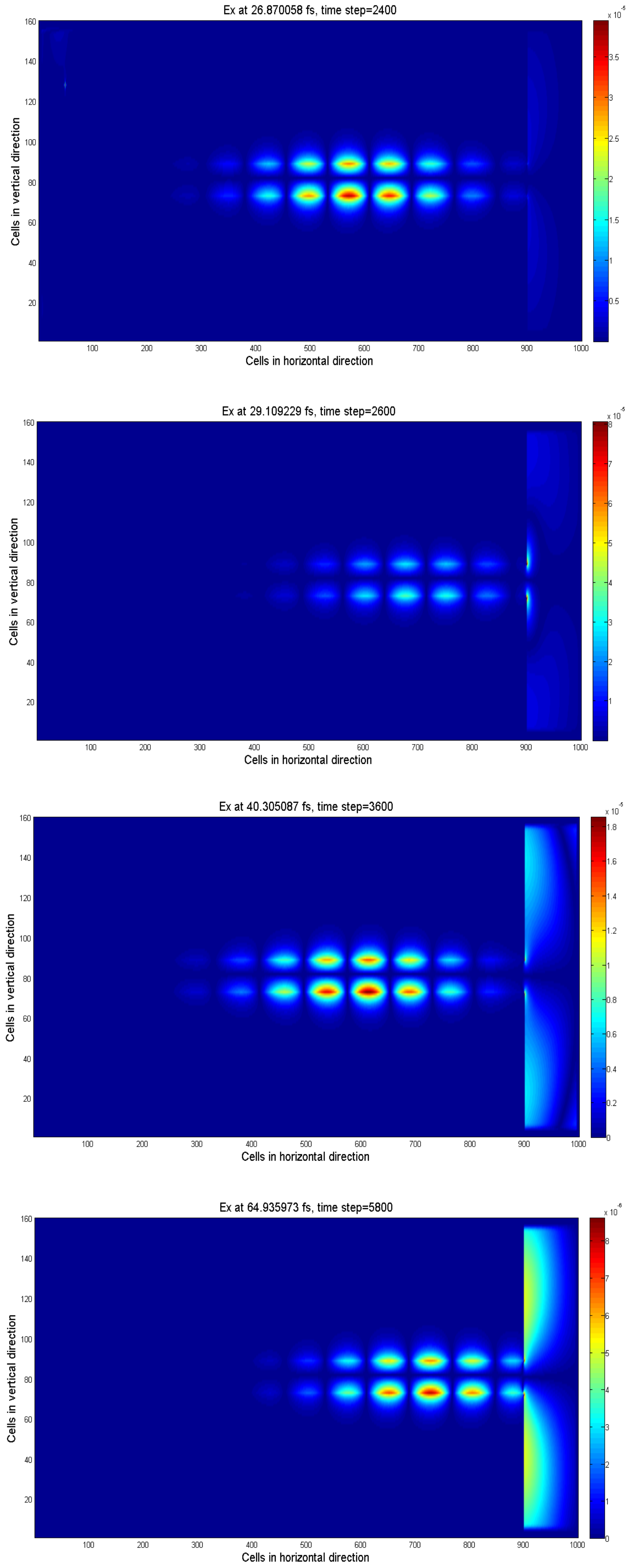

Figure 6-7: 4 snapshots of Ex field distribution at the Ag-air-Ag interface

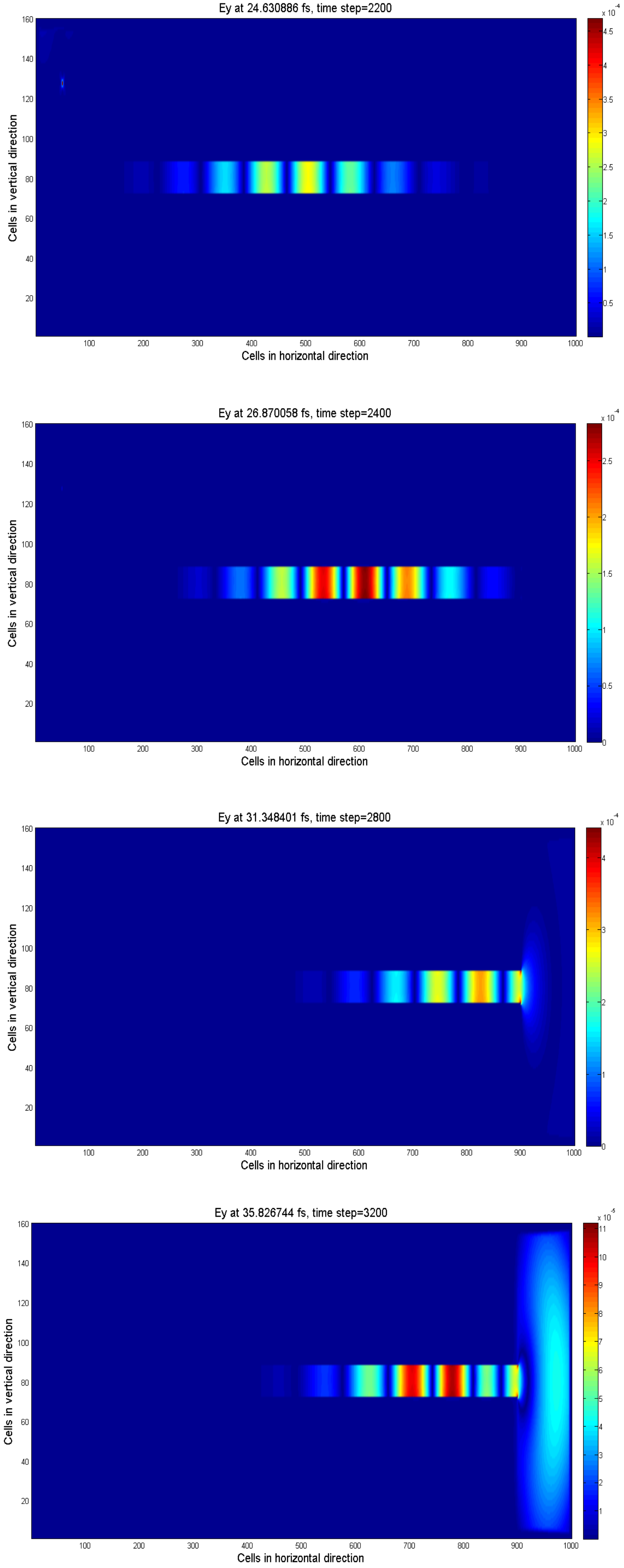

Figure 6-8: 4 snapshots of Ey field distribution at the Ag-air-Ag interface

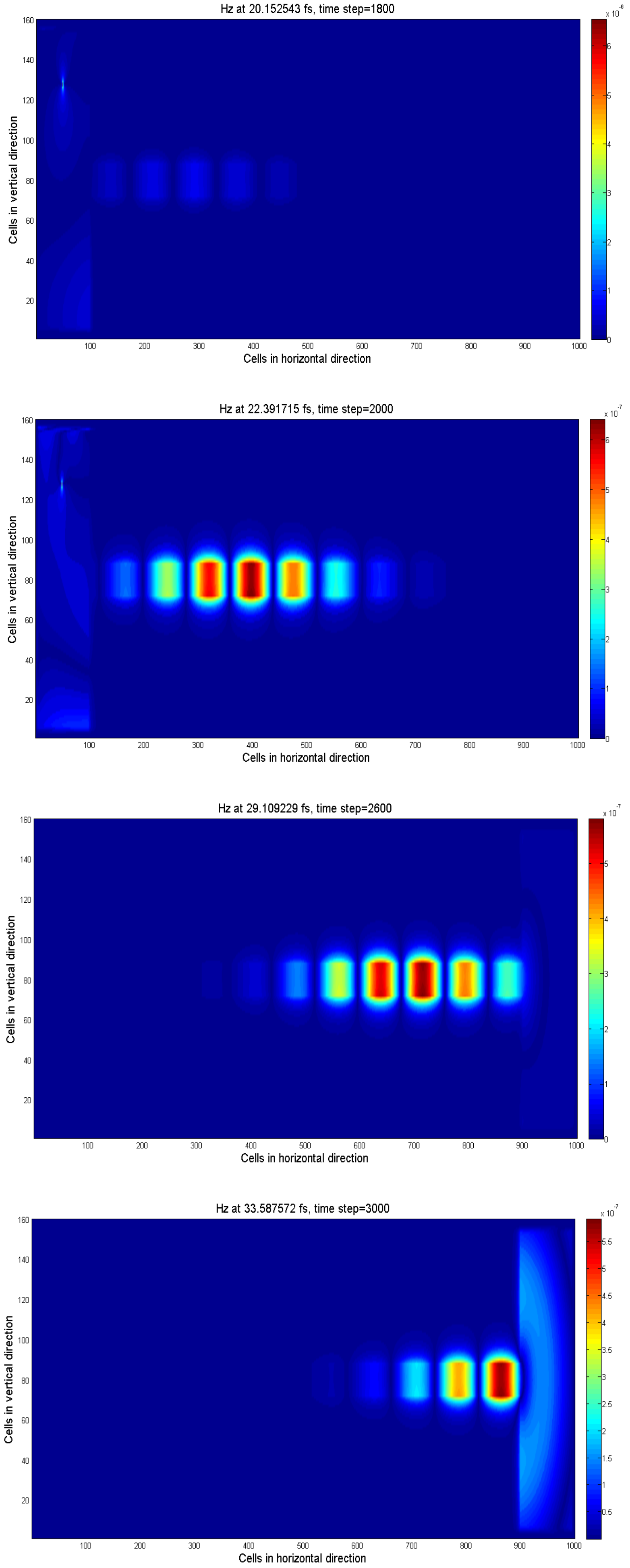

Figure 6-9: 4 snapshots of Hz field distribution at the Ag-air-Ag interface

6.5 Power Calculation in Silver-Alumina-Silver Waveguide

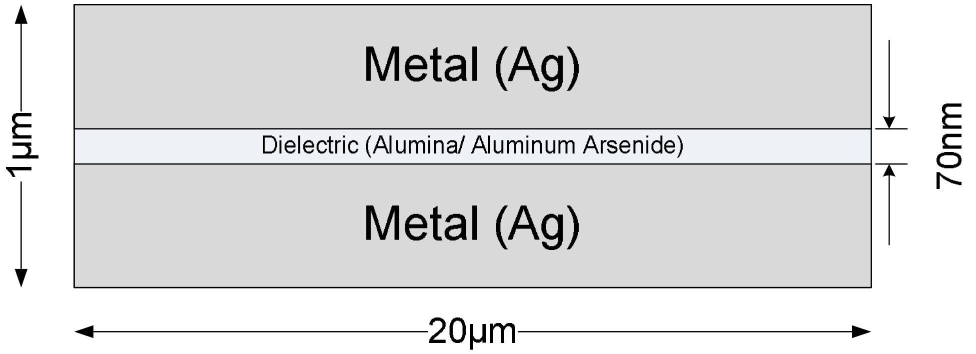

Figure 6-12: MDM waveguide for SPP propagation.

A layer of alumina/ aluminum arsenide is sandwiched between two layers of silver to form a metal-dielectric-metal (MDM) waveguide. The modeling parameters of alumina and aluminum arsenide are extracted based on the Lorentz model using the algorithm described in chapter 5.

The modeling parameters of alumina are:

$\varepsilon_\infty = 1.001$

$\Delta\varepsilon_1 = 2.057793$

$\delta_1 = 2.7 \times 10^{12}$rad/sec

$\omega_1 = 1.9678 \times 10^{16}$rad/sec

Applicability range: 200-1960nm

The modeling parameters of aluminum arsenide are:

$\varepsilon_\infty = 2.642392$

$\Delta\varepsilon_1 = 5.5635$

$\delta_1 = 1.885 \times 10^{12}$rad/sec

$\omega_1 = 6.243 \times 10^{15}$rad/sec

Applicability range: 500-1770nm

The distribution of the E_y field of the symmetric SPP mode propagating through the MDM waveguide is shown in figure 6-13. The normalized power curves for Al_2O_3 and AlAs are shown in figure 6-14. From the curves we see that the attenuation of SPP is less if Al_2O_3 is used as a dielectric layer in the MDM waveguide compared to AlAs.

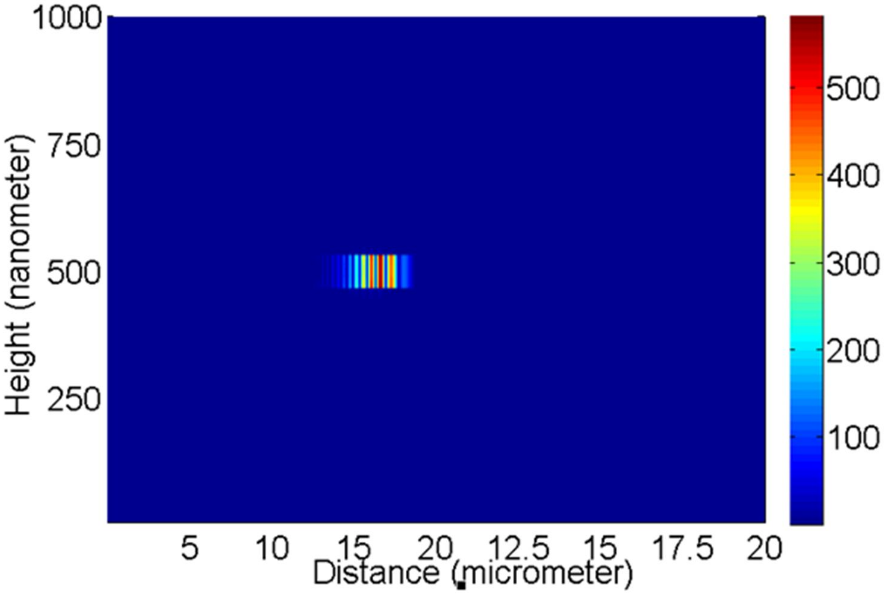

Figure 6-13: E_y field distribution inside the waveguide.

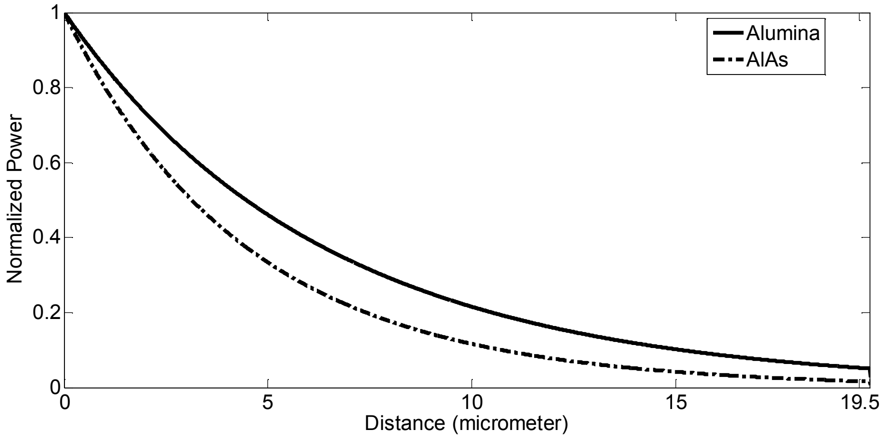

Figure 6-14: Normalized power profile through the MDM waveguide.

From the simulation of Ag/AlAs/Ag and Ag/Al_2O_3/Ag waveguides we can conclude that compared to AlAs, Al_2O_3 is a better choice as dielectric layer in MDM waveguide in terms of attenuation. In order to completely characterize the performance of AlAs and Al_2O_3 as dielectric layers in MDM waveguide we also need to consider the confinement factor which is left as future work . Using the same procedure, other materials and configurations can be simulated to compare their performance as SPP waveguides.

6.6 Simulation of Periodic Array of Metal on Air Substrate

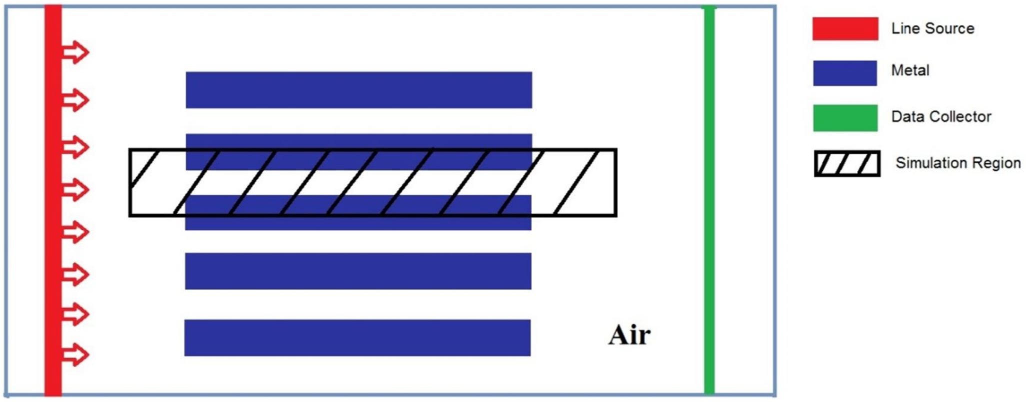

Figure 6-15: Periodic array of metal on air substrate

A periodic array of metal layers on air substrate as shown in figure 6-14 is simulated. Since the array of metal layer is periodic, instead of simulating the whole structure, only one period of it is simulated. In the simulation we have used four different metals- aluminum, silver, gold and platinum. Power is calculated at the output section of the structure and is divided by the input power to get the transmittance.

The transmittance curves for the four metals are shown in figure 6-15.

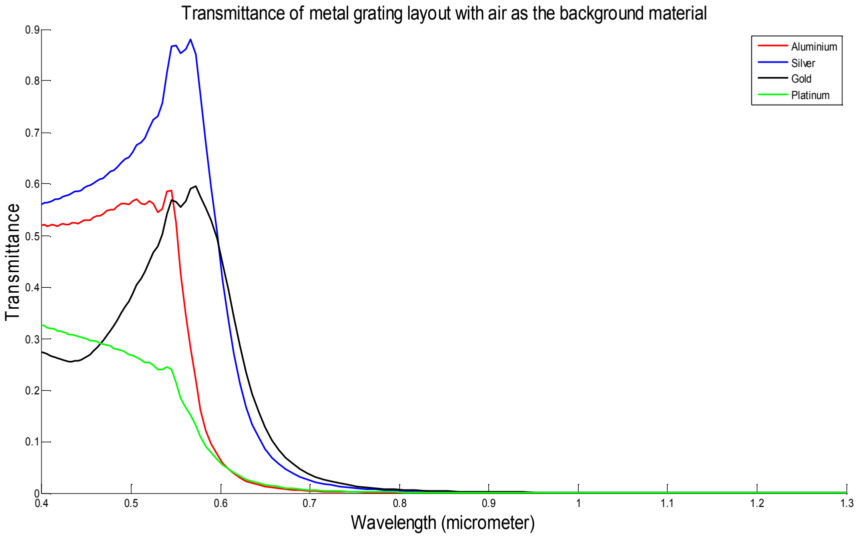

Figure 6-16: Transmittance of metal grating layout with air as the background material

From the transmittance curves it is evident that this type of structure acts as low pass filter is terms of wavelength.

6.7 Simulation of Sub-wavelength Holes in Gold Film

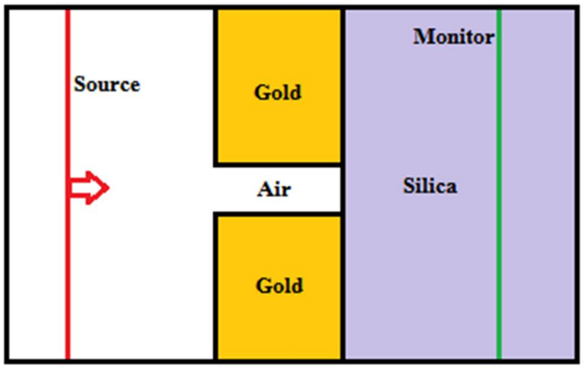

Figure 6-17: Sub-wavelength hole in gold film deposited on silica

Under normal conditions, light cannot travel through holes or gaps below the diffraction limit. One of the main advantages of SPPs is that they can overcome this diffraction limit. This fact is verified using simulation.

The diffraction limit is given by

$$d \approx \frac{\lambda}{2n \sin \alpha}$$

where λ is the wavelength in meter

n is the refractive index (dimensionless)

α is the angle of incidence.

d is diffraction limit distance in meter

For air n=1. For normal incidence α=90°.

So, $d = \frac{\lambda}{2}$

We have performed simulation with the wavelength range of 500-1000nm. So, the diffraction limit is 250-500nm.

The simulation structure is shown in figure 6-16. The air gap shown in the structure has a width D. We have used six different values of D (138.5nm, 130nm, 119nm, 114.5nm, 97nm and 89nm) all of which are less than 340nm. In all cases, we observed some power being propagated to the silica layer as shown by the power transmission spectrum in figure 6-17.

This proves the ability of SPPs to overcome diffraction limit.

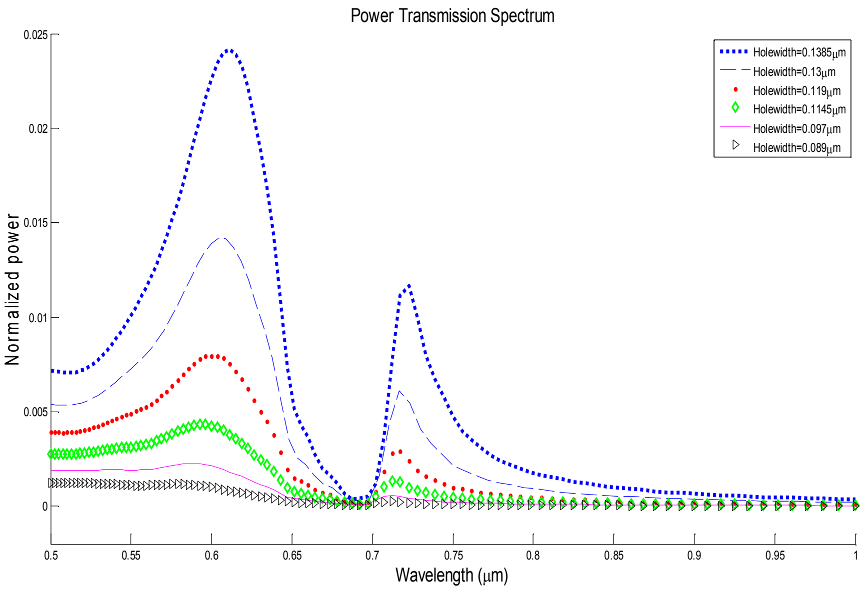

Figure 6-18: Power transmission spectrum for the structure shown in 6-17

Chapter 7

Conclusion and Future Works

We have extracted the modeling parameters of several linear dispersive materials. Among them we have used alumina and aluminum arsenide for simulation of an MDM waveguide. Besides, we have developed a simulation model for analyzing plasmonic nanostructure and have simulated SPP propagation through single metal dielectric interface, periodic array of metal on air substrate and have verified the ability of SPPs to overcome diffraction limit.

Any linear dispersive material can be modeled using the optimization method we have used. We hope to use different materials to construct different plasmonic structures and analyze their performance in future.

Plasmon enhanced and plasmonic solar cells are two promising application of Plasmonics which we hope to explore in future.

REFERENCES:

[1] M. Pelton and G. W. Bryant, *Introduction to metal-nanoparticle plasmonics* vol. 5: John Wiley & Sons, 2013.

[2] A. Al-Azzawi, *Light and optics: principles and practices*: CRC Press, 2006.

[3] D. A. Pucknell and K. Eshraghian, *Basic VLSI design: systems and circuits*: Prentice-Hall, Inc., 1988.

[4] J. J. Parsons and D. Oja, "New Perspectives on Computer Concepts 2014, Enhanced, Brief (Book Only)," 2014.

[5] M. Diwekar, *Studies on Two-dimensional Metallic Photonic Crystals and Magnetic Properties of Patterned Superconducting Films*: ProQuest, 2007.

[6] S. A. Maier, *Plasmonics: Fundamentals and Applications: Fundamentals and Applications*: Springer, 2007.

[7] H. A. Atwater, "The promise of plasmonics," *Scientific American*, vol. 296, pp. 56-62, 2007.

[8] M. R. Gartia, *et al.*, "Colorimetric plasmon resonance imaging using nano lycurgus cup arrays," *Advanced Optical Materials*, vol. 1, pp. 68-76, 2013.

[9] M. Beech, *The Physics of Invisibility: A Story of Light and Deception*: Springer, 2011.

[10] K. Catchpole and A. Polman, "Plasmonic solar cells," *Optics Express*, vol. 16, pp. 21793-21800, 2008.

[11] A. Deinega and S. John, "Effective optical response of silicon to sunlight in the finite-difference time-domain method," *Optics letters*, vol. 37, pp. 112-114, 2012.

[12] A. D. Rakic, *et al.*, "Optical properties of metallic films for vertical-cavity optoelectronic devices," *Applied optics*, vol. 37, pp. 5271-5283, 1998.

[13] R. H. Sagor, *et al.*, "An optimization method for parameter extraction of metals using modified Debye model," *SpringerPlus*, vol. 2, p. 426, 2013.

[14] M. G. Saber and R. H. Sagor, "Optimization of the optical properties of cuprous oxide and silicon-germanium alloy using the Lorentz and Debye models," *Electronic Materials Letters*, vol. 10, pp. 267-269, 2014.

[15] M. Alsunaidi and F. Al-Hajiri, "Time-domain Analysis of Wideband Optical Pulse SHG in Layered Dispersive Material," *Session 5A1 Optics and Photonics*, vol. 2, p. 795.

[16] M. A. Ordal, *et al.*, "Optical properties of fourteen metals in the infrared and far infrared: Al, Co, Cu, Au, Fe, Pb, Mo, Ni, Pd, Pt, Ag, Ti, V, and W," *Applied optics*, vol. 24, pp. 4493-4499, 1985.

[17] W. Saj, "FDTD simulations of 2D plasmon waveguide on silver nanorods in hexagonal lattice," *Optics Express*, vol. 13, pp. 4818-4827, 2005.

[18] T. Onuki, *et al.*, "Propagation of surface plasmon polariton in nanometre-sized metal-clad optical waveguides," *Journal of microscopy*, vol. 210, pp. 284-287, 2003.

[19] M. Hochberg, *et al.*, "Integrated plasmon and dielectric waveguides," *Optics Express*, vol. 12, pp. 5481-5486, 2004.

[20] K. Hasegawa, *et al.*, "Curvature-induced radiation of surface plasmon polaritons propagating around bends," *Physical Review A*, vol. 75, p. 063816, 2007.

[21] X. Zhai, *et al.*, "A subwavelength plasmonic waveguide filter with a ring resonator," *Journal of Nanomaterials*, vol. 2013, 2013.

[22] T.-B. Wang, *et al.*, "The transmission characteristics of surface plasmon polaritons in ring resonator," *Optics Express*, vol. 17, pp. 24096-24101, 2009.

[23] J. Vuckovic, *et al.*, "Surface plasmon enhanced light-emitting diode," *Quantum Electronics, IEEE Journal of*, vol. 36, pp. 1131-1144, 2000.

[24] S. Pillai, *et al.*, "Surface plasmon enhanced silicon solar cells," *Journal of applied physics*, vol. 101, p. 093105, 2007.

[25] A. Taflove and S. C. Hagness, "Computational Electrodynamics: the FDTD method," *Artech House Boston, London*, 2000.

[26] A. Taflove and S. C. Hagness, "Computationai Electrodynamics," 2000.

[27] J. Takahara and F. Kusunoki, "Guiding and nanofocusing of two-dimensional optical beam for nanooptical integrated circuits," *IEICE Transactions on Electronics,* vol. 90, pp. 87-94, 2007.
[28] C. R. Pollock and M. Lipson, *Integrated photonics* vol. 20: Springer, 2003.
[29] R. M. Joseph, *et al.*, "Direct time integration of Maxwell's equations in linear dispersive media with absorption for scattering and propagation of femtosecond electromagnetic pulses," *Optics letters,* vol. 16, pp. 1412-1414, 1991.
[30] L. Frank, *et al.*, "Introduction to optics," ed: Prentice-Hall International Inc., New York, 1993.
[31] X. Zhang and Z. Liu, "Superlenses to overcome the diffraction limit," *Nature materials,* vol. 7, pp. 435-441, 2008.
[32] A. Deinega, *et al.*, "Optimization of an anti-reflective layer of solar panels based on ab initio calculations," *Russian Physics Journal,* vol. 52, pp. 1128-1134, 2009.
[33] E. K. Chong and S. H. Zak, *An introduction to optimization* vol. 76: John Wiley & Sons, 2013.
[34] S. Adachi, *Optical constants of crystalline and amorphous semiconductors: numerical data and graphical information*: Springer, 1999.
[35] S. Adachi, *The Handbook on Optical Constants of Semiconductors: In Tables and Figures*: World Scientific, 2012.
[36] S. Adachi, *The Handbook on Optical Constants of Metals: In Tables and Figures*: World Scientific Publishing Company Pte Limited, 2012.
[37] D. Aspnes and A. Studna, "Dielectric functions and optical parameters of si, ge, gap, gaas, gasb, inp, inas, and insb from 1.5 to 6.0 ev," *Physical Review B,* vol. 27, p. 985, 1983.
[38] E. D. Palik, *Handbook of Optical Constants of Solids*: Academic Press, 1998.
[39] R. Barati, "Parameter estimation of nonlinear Muskingum models using Nelder-Mead simplex algorithm," *Journal of Hydrologic Engineering,* vol. 16, pp. 946-954, 2011.
[40] K. S. Yee, "Numerical solution of initial boundary value problems involving Maxwell's equations in isotropic media," *IEEE Trans. Antennas Propag,* vol. 14, pp. 302-307, 1966.
[41] M. A. Alsunaidi and A. A. Al-Jabr, "A general ADE-FDTD algorithm for the simulation of dispersive structures," *Photonics Technology Letters, IEEE,* vol. 21, pp. 817-819, 2009.
[42] J.-P. Berenger, "A perfectly matched layer for the absorption of electromagnetic waves," *Journal of computational physics,* vol. 114, pp. 185-200, 1994.
[43] R. H. Sagor, "Plasmon enhanced symmetric mode generation in metal-insulator-metal structure with Kerr nonlinear effect," *International Journal of Computer Applications,* vol. 50, pp. 24-28, 2012.